



CERN-EP-XXXX-XXX  
Day Month XXXX

# Non-linear flow modes of identified particles in Pb–Pb collisions at $\sqrt{s_{\text{NN}}} = 5.02 \text{ TeV}$

ALICE Collaboration\*

## Abstract

The  $p_{\text{T}}$ -differential non-linear flow modes,  $v_{4,22}$ ,  $v_{5,32}$ ,  $v_{6,33}$  and  $v_{6,222}$  for  $\pi^{\pm}$ ,  $K^{\pm}$ ,  $K_S^0$ ,  $p + \bar{p}$ ,  $\Lambda + \bar{\Lambda}$  and  $\phi$ -meson have been measured for the first time in Pb–Pb collisions at  $\sqrt{s_{\text{NN}}} = 5.02 \text{ TeV}$  with the ALICE detector at the Large Hadron Collider. The results were obtained with a multi-particle technique, correlating the identified hadrons with reference particles from a different pseudorapidity region. These non-linear observables probe the contribution of the second and third order symmetry plane angles in higher flow harmonics. All the characteristic features observed in previous  $p_{\text{T}}$ -differential measurements (e.g.  $v_2$  and  $v_3$ ) for various particle species are also present in the measurement of the non-linear flow modes, i.e. increase of magnitude with increasing the centrality percentile, mass ordering at low  $p_{\text{T}}$  and particle type grouping in the intermediate  $p_{\text{T}}$  range. Hydrodynamical calculations (iEBE-VISHNU) that use different initial conditions and values of shear and bulk viscosity to entropy density ratios are confronted with the data at low transverse momenta. This comparison provides ~~new~~additional discriminatory power in the study of initial conditions as well as new stringent constraints to hydrodynamical calculations.

20	<b>Contents</b>	
21	<b>1 Introduction</b>	<b>3</b>
22	<b>2 Experimental setup</b>	<b>5</b>
23	<b>3 Event sample, track selection and particle identification</b>	<b>7</b>
24	3.1 Trigger selection and data sample . . . . .	7
25	3.2 Selection of primary $\pi^\pm$ , $K^\pm$ and $p + \bar{p}$ . . . . .	7
26	3.3 Reconstruction of $K_S^0$ , $\Lambda + \bar{\Lambda}$ and $\phi$ meson . . . . .	8
27	<b>4 Analysis method</b>	<b>9</b>
28	<b>5 Systematic uncertainties</b>	<b>10</b>
29	<b>6 Results and discussion</b>	<b>13</b>
30	6.1 Centrality and $p_T$ dependence of non-linear flow modes . . . . .	13
31	6.2 Comparison with models . . . . .	16
32	6.3 <a href="#"><u>Comparison with <math>v_n</math> of identified particles</u></a> . . . . .	22
33	<b>7 Summary</b>	<b>24</b>
34	<b>A Additional figures</b>	<b>33</b>
35	A.1 $K_{ET}$ scaling . . . . .	33
36	<b>B The ALICE Collaboration</b>	<b>33</b>

## 1 Introduction

Lattice quantum chromodynamics (QCD) calculations [1, 2] suggest that at extremely high temperature and energy density a state of matter is produced in which quarks and gluons are no longer confined into hadrons. This state of matter is called quark-gluon plasma (QGP) [3–5]. The main goal of heavy-ion collision experiments is to study the properties of the QGP, such as the speed of the sound, the equation of state and its shear and bulk viscosities.

One of the observables sensitive to the properties of the QGP is the azimuthal angular distribution of particles emitted in the plane perpendicular to the beam axis. In a heavy ion collision, the overlap region of the colliding nuclei exhibits an irregular shape [6–10]. This spatial irregularity is a superposition of the geometry, i.e. centrality of the collision reflected in the value of the impact parameter, and the ~~density profile of nucleons participating in the collision~~ initial energy density in the transverse plane. Through interactions between partons and at later stages between the produced particles, this spatial irregularity is transferred into an anisotropy in momentum space. The latter is usually expressed by a Fourier expansion of the azimuthal particle distribution ~~[11?]~~ [11] according to

$$\frac{dN}{d\phi} \propto 1 + 2 \sum_{n=1}^{\infty} v_n(p_T) \cos[n(\phi - \Psi_n)], \quad (1)$$

where  $N$ ,  $p_T$  and  $\phi$  are the particle yield, transverse momentum and azimuthal angle of particles, respectively, and  $\Psi_n$  is the azimuthal angle of the symmetry plane of the  $n^{\text{th}}$ -order coefficient ~~[6–9]~~ [6–9, 12]. The parameter  $v_n$  is the magnitude of the  $n^{\text{th}}$ -order complex flow coefficient  $V_n$ , defined as  $V_n = v_n e^{in\Psi_n}$ , and can be calculated according to

$$v_n = \langle \cos[n(\phi - \Psi_n)] \rangle, \quad (2)$$

where the brackets denote an average over all particles in ~~all events~~ an event. Since the symmetry planes are not accessible experimentally, the flow coefficients are estimated solely from the azimuthal angles of the particles emitted in the transverse plane. Measurements of different anisotropic flow coefficients at both RHIC ~~[13–16]~~ [13–29] and the LHC ~~[37, 38, 40]~~ [30–40] have not only confirmed the production of a strongly coupled quark gluon plasma (sQGP) but they have also constrained the value of its shear viscosity over entropy density ( $\eta/s$ ) very close to the lower limit of  $1/4\pi$  conjectured by AdS/CFT [41]. In addition, the comparison between experimental data [39] and viscous hydrodynamical calculations [42] show that higher order flow coefficients and more importantly their transverse momentum dependence are more sensitive probes than lower order coefficients, i.e.  $v_2$  and  $v_3$ , of the initial spatial irregularity and its fluctuations [9].

This initial state spatial irregularity can be quantified with the standard (moment-based) anisotropy coefficients,  $\epsilon_n$ . Together with their corresponding initial symmetry planes,  $\Phi_n$ ,  $\epsilon_n$  can be calculated from the transverse positions of the nucleons participating in a collisions according to [43, 44]

$$\epsilon_n e^{in\Phi_n} = \frac{\langle r^n e^{in\phi} \rangle}{\langle r^n \rangle} \text{ (for } n > 1), \quad (3)$$

where the brackets denote an average over the transverse position of all participating nucleons that have an azimuthal angle  $\phi$  and a polar distance from the centre  $r$ . Model calculations show that  ~~$V_2$~~   $v_2$  and to a large extent,  ~~$V_3$  are determined by  $v_3$~~   $v_3$  are linearly proportional to their corresponding initial spatial anisotropy coefficients,  $\epsilon_2$  and  $\epsilon_3$ , respectively [8]. ~~It has been realised that for  $n > 3$ ,  $V_n$  are not linearly correlated with their corresponding  $\epsilon_n$  [9, 46].~~ while for larger values of  $n$ , nonlinearities are observed, i.e.  $v_n \propto \epsilon_n$  [9]. In fact, a cumulant-based definition of initial anisotropic coefficient suggests additional

terms in the definition of  $\varepsilon_n$  for higher order flow coefficients ( $n > 3$ ). As an example, the fourth order spatial anisotropy is given by

$$\varepsilon'_4 e^{i4\Phi'_4} = \varepsilon_4 e^{i4\Phi_4} + \frac{3\langle r^2 \rangle^2}{\langle r^4 \rangle} \varepsilon_2^2 e^{i4\Phi_2}, \quad (4)$$

where  $\varepsilon'_4$  is the cumulant-based spatial anisotropy coefficient [44, 45]. This dependence on lower order initial anisotropies gives rise to additional terms in the higher order flow coefficients. As a result,  $V_n$  ( $n > 3$ ) obtain contributions not only from the linear response of the system to  $\varepsilon_n$ , but also a non-linear response proportional to the product of lower order initial spatial anisotropies [46, 47].

In particular, for a single event,  $V_n$  with  $n = 4, 5, 6$  can be decomposed to the linear ( $V_n^L$ ) and non-linear ( $V_n^{NL}$ ) modes according to

$$\begin{aligned} V_4 &= V_4^L + V_4^{NL} = V_4^L + \chi_{4,22}(V_2)^2, \\ V_5 &= V_5^L + V_5^{NL} = V_5^L + \chi_{5,32}V_3V_2, \\ V_6 &= V_6^L + V_6^{NL} = V_6^L + \chi_{6,222}(V_2)^3 + \chi_{6,33}(V_3)^2 + \chi_{6,42}V_2V_4^L, \end{aligned} \quad (5)$$

where  $\chi_{n,mk}$ , known as non-linear flow mode coefficients, quantify the contributions of the non-linear modes to the total  $V_n$  [47, 48]. The magnitude of the  $p_T$ -differential non-linear modes in higher order flow coefficients,  $v_n^{NL}$ , can be written as:

$$v_{4,22}(p_T) = \frac{\langle v_4(p_T)v_2^2 \cos(4\Psi_4 - 4\Psi_2) \rangle}{\sqrt{\langle v_2^4 \rangle}} \approx \langle v_4(p_T) \cos(4\Psi_4 - 4\Psi_2) \rangle, \quad (6)$$

$$v_{5,32}(p_T) = \frac{\langle v_5(p_T)v_3v_2 \cos(5\Psi_5 - 3\Psi_3 - 2\Psi_2) \rangle}{\sqrt{\langle v_3^2v_2^2 \rangle}} \approx \langle v_5(p_T) \cos(5\Psi_5 - 3\Psi_3 - 2\Psi_2) \rangle, \quad (7)$$

$$v_{6,33}(p_T) = \frac{\langle v_6(p_T)v_3^2 \cos(6\Psi_6 - 6\Psi_3) \rangle}{\sqrt{\langle v_3^4 \rangle}} \approx \langle v_6(p_T) \cos(6\Psi_6 - 6\Psi_3) \rangle, \quad (8)$$

$$v_{6,222}(p_T) = \frac{\langle v_6(p_T)v_2^3 \cos(6\Psi_6 - 6\Psi_2) \rangle}{\sqrt{\langle v_2^6 \rangle}} \approx \langle v_6(p_T) \cos(6\Psi_6 - 6\Psi_2) \rangle, \quad (9)$$

where brackets denote an average over all events. The approximation is valid assuming a weak correlation between the lower ( $n = 2, 3$ ) and higher ( $n > 3$ ) order flow coefficients.

Various measurements of the  $p_T$ -differential anisotropic flow,  $v_n(p_T)$ , of charged particles at the LHC [31, 36, 49, 50] have provided a testing ground for hydrodynamical calculations that attempt to describe the dynamical evolution of the system created in heavy-ion collisions. Early predictions showed that  $p_T$ -differential anisotropic flow for different particle species can reveal more information about the equation of state and hadronic rescattering phase [51, 52] as well as particle production mechanisms. In order to test these predictions,  $v_n(p_T)$  have been measured for different particle species at the LHC [37, 38, 40, 53] and RHIC [13–16]. These measurements have revealed that an interplay between radial flow and anisotropic flow leads to a characteristic mass dependence in the low transverse momentum ( $p_T$ ) region ( $p_T < 3$  GeV/ $c$ ). For higher values of  $p_T$  (up to 6 GeV/ $c$ ) results indicate a particle type grouping where baryons have a larger  $v_n$  magnitude than the one of mesons. This feature was explained in a dynamical model where flow develops at the partonic level followed by quark coalescence into hadrons [54, 55].

This model assumes that the invariant spectrum of produced particles is proportional to the product of the spectra of their constituents and, in turn, the flow coefficients of produced particles is the sum of the  $v_n$  values of its constituents. Measurements of lower order total flow coefficients exhibit number of constituent quarks (NCQ) scaling at RHIC [56] and the LHC [37, 38] at an approximate level of  $\pm 20\%$  for  $p_T > 3$  GeV/c.

The measurements of non-linear flow modes in different collision geometries challenge hydrodynamic models and have the potential to further constrain both the initial conditions of the collision system and its transport properties [48][48, 57]. The  $p_T$ -dependent non-linear flow modes of identified particles are important observable for studying the characteristics of QGP. They not only put a stringent constraint on both the initial conditions of the collision system and its transport properties, i.e.  $\eta/s$  and  $\zeta/s$ , but also allow to test the effect of late-stage interactions in the hadronic rescattering phase as well as the effect of particle production via the coalescence mechanism to the development of the mass ordering and particle type grouping [31, 40].

In this article, we report the first results of the  $p_T$ -differential non-linear flow modes,  $v_{4,22}$ ,  $v_{5,32}$ ,  $v_{6,33}$  and  $v_{6,222}$  for  $\pi^\pm$ ,  $K^\pm$ ,  $K_S^0$ ,  $p + \bar{p}$ ,  $\Lambda + \bar{\Lambda}$  and  $\phi$  measured in Pb–Pb collisions at a centre of mass energy per nucleon pair  $\sqrt{s_{NN}} = 5.02$  TeV, recorded with the ALICE detector [58] at the LHC. The detectors and the selection criteria used in this analysis are described in Sec. 2 and 3, respectively. The analysis methodology and technique is presented in Section 4. In this article, the identified hadron under study and the charged reference particles are obtained from different, non-overlapping pseudorapidity regions. The correlations not related to the common symmetry plane (known as non-flow), like those arising from jets, resonance decays and quantum statistics correlations, are suppressed by using multi-particle correlations as explained in Section 4 and the residual effect is assigned as a systematic uncertainty, described in Section 5. All coefficients for charged particles were measured separately for particles and anti-particles and were found to be compatible within statistical uncertainties. The reported measurements are therefore an average of the results for the opposite charges. The results are reported within the pseudorapidity range  $|\eta| < 0.8$  at different collision centralities between 0–60% range of Pb–Pb collisions.

## 2 Experimental setup

ALICE [58, 59] is one of the four large experiments at the LHC, particularly designed to cope with the large charged-particle densities present in central Pb–Pb collisions [60]. By convention, the  $z$ -axis is parallel to the beam direction, the  $x$ -axis is horizontal and points towards the centre of the LHC, and the  $y$ -axis is vertical and points upwards. The apparatus consists of a set of detectors located in the central barrel, positioned inside a solenoidal magnet which generates a 0.5 T field parallel to the beam direction, and a set of forward detectors.

The Inner Tracking System (ITS) [58] and the Time Projection Chamber TPC [61] are the main tracking detectors of the central barrel. The ITS consists of six layers of silicon detectors employing three different technologies. The two innermost layers, positioned at  $r = 3.9$  cm and 7.6 cm, are Silicon Pixel Detectors (SPD), followed by two layers of Silicon Drift Detectors (SDD) ( $r = 15$  cm and 23.9 cm). Finally, the two outermost layers are double-sided Silicon Strip Detectors (SSD) at  $r = 38$  cm and 43 cm. The TPC has a cylindrical shape with an inner radius of about 85 cm, an outer radius of about 250 cm, and a length of 500 cm and it is positioned around the ITS. It provides full azimuthal coverage in the pseudorapidity range  $|\eta| < 0.9$ .

Charged particles were identified using the information from the TPC and the TOF detectors [58]. The TPC allows for a simultaneous measurement of the momentum of a particle and its specific energy loss  $\langle dE/dx \rangle$  in the gas. The detector provides a separation more than 2 standard deviations for the hadron species at  $p_T < 0.7$  GeV/c and the possibility to identify particles on a statistical basis in the relativistic rise region of  $dE/dx$  (i.e.  $2 < p_T < 20$  GeV/c) [59]. The  $dE/dx$  resolution for the 5% most central

Pb–Pb collisions is 6.5% and improves for more peripheral collisions. The TOF detector is situated at a radial distance of 3.7 m from the beam axis, around the TPC and provides a  $3\sigma$  separation between  $\pi$ –K and K–p up to  $p_T = 2.5$  GeV/ $c$  and  $p_T = 4$  GeV/ $c$ , respectively [59]. This is done by measuring the flight time of particles from the collision point with a resolution of about 80 ps. The start time for the TOF measurement is provided by the T0 detectors, two arrays of Cherenkov counters positioned at opposite sides of the interaction points covering  $4.6 < \eta < 4.9$  (T0A) and  $-3.3 < \eta < -3.0$  (T0C). The start time is also determined using a combinatorial algorithm that compares the timestamps of particle hits measured by the TOF to the expected times of the tracks, assuming a common event time  $t_{ev}$  [59]. Both methods of estimating the start time are fully efficient for Pb–Pb collisions up to 80% centrality interval.

A set of forward detectors, the V0 scintillator arrays [62], were used in the trigger logic and for the determination of the collision centrality. The V0 consists of two detectors, the V0A and the V0C, positioned on each side of the interaction point, covering the pseudorapidity ranges of  $2.8 < \eta < 5.1$  and  $-3.7 < \eta < -1.7$ , respectively.

For more details on the ALICE apparatus and the performance of the detectors, see Refs. [58, 59].

### 3 Event sample, track selection and particle identification

#### 3.1 Trigger selection and data sample

The analysis is performed on minimum bias Pb–Pb collision data at  $\sqrt{s_{NN}} = 5.02$  TeV collected by ALICE in 2015. These events were triggered by the coincidence between signals from both V0A and V0C detectors. An offline event selection, exploiting the signal arrival time in V0A and V0C, measured with a 1 ns resolution, was used to discriminate beam induced-background (e.g. beam gas events) from collision events. This led to a reduction of background events in the analysed samples to a negligible fraction ( $< 0.1\%$ ) [59]. Events with multiple reconstructed vertices were rejected by comparing multiplicity estimates from the V0 detector to tracking detectors at mid-rapidity, exploiting the difference in readout times between the systems. The fraction of pileup events left after applying the dedicated pileup removal criteria is negligible. All events selected for the analysis had a reconstructed primary vertex position along the beam axis ( $z_{vtx}$ ) within 10 cm from the nominal interaction point. After all the selection criteria, a filtered data sample of approximately 40 million Pb–Pb events in 0-60% centrality interval was analysed to produce the results presented in this article.

Events were classified according to fractions of the ~~inelastic-total~~ nucleus-nucleus cross section. The 0-5% interval represents the most central interactions (i.e. smallest impact parameter) and is referred to as most central collisions. On the other hand, the 50-60% centrality interval corresponds to the most peripheral (i.e. largest impact parameter) collisions in the analysed sample. The centrality of the collision was estimated using the energy deposition measured in the V0 detectors. Details about the centrality determination can be found in Ref. [63].

#### 3.2 Selection of primary $\pi^\pm$ , $K^\pm$ and $p + \bar{p}$

In this analysis, tracks are reconstructed using the information from the TPC and the ITS detectors. The tracking algorithm, based on the Kalman filter [64, 65], starts from a collection of space points (referred to as clusters) inside the TPC, and provides the quality of the fit by calculating its  $\chi^2$  value. Each space point is reconstructed at one of the TPC padrows, where the deposited ionisation energy is also measured. The specific ionisation energy loss  $\langle dE/dx \rangle$  is estimated using a truncated mean, excluding the 40% highest-charge clusters associated to the track. The obtained  $\langle dE/dx \rangle$  has a resolution, which we later refer to as  $\sigma_{TPC}$ . The tracks are propagated to the outer layer of the ITS, and the tracking algorithm attempts to identify space points in each one of the consecutive layers, reaching the innermost ones (i.e. SPD). The track parameters are then updated using the combined information from both the TPC and the ITS detectors.

Primary charged pions, kaons and (anti-)protons were required to have at least 70 reconstructed space points out of the maximum of 159 in the TPC. The average of the track fit per TPC space point per degree of freedom (see [59] for details) was required to be below 4. These selections reduce the contribution from short tracks, which are unlikely to originate from the primary vertex. To further reduce the contamination by secondary tracks from weak decays or from the interaction with the material, only particles within a maximum distance of closest approach (DCA) between the tracks and the primary vertex in both the transverse plane ( $DCA_{xy} < 0.0105 + 0.0350(p_T \text{ c/GeV})^{-1.1}$  cm) and the longitudinal direction ( $DCA_z < 2$  cm) were analysed. Moreover, the tracks were required to have at least two associated ITS clusters in addition to having a hit in either of the two SPD layers. This selection leads to an efficiency of about 80% for primary tracks at  $p_T < 0.6$  GeV/c and a contamination from secondaries of about 5% at  $p_T = 1$  GeV/c [66]. These values depend on particle species and transverse momentum [66]. These selection criteria are listed in Tab. 1. Relevant selection criteria for tracks used for the reconstruction of  $K_S^0$ ,  $\Lambda + \bar{\Lambda}$  and  $\phi$ -meson are given in Sec. 3.3.

The particle identification (PID) for pions ( $\pi^\pm$ ), kaons ( $K^\pm$ ) and protons ( $p + \bar{p}$ ) used in this analysis relies on the two-dimensional correlation between the number of standard deviations in units of the

resolution from the expected signals of the TPC and the TOF detectors similar to what was reported in [37, 38, 40]. In this approach particles were selected by requiring their standard deviations from the  $\langle dE/dx \rangle$  and  $t_{\text{TOF}}$  values to be less than a  $p_T$ -dependent value, maintaining a minimum purity of 90% for  $\pi^\pm$ , 75% for  $K^\pm$  and 80% for  $p + \bar{p}$ . In order to further reduce the contamination from other species, the standard deviation of a given track was required to be the minimum among other candidate species.

In addition, for the systematics (see section 5) the minimum purity was required to be 80%, a condition that becomes essential with increasing transverse momentum where the relevant detector response for different particle species starts to overlap.

### 3.3 Reconstruction of $K_S^0$ , $\Lambda + \bar{\Lambda}$ and $\phi$ meson

In this analysis, the  $K_S^0$  and  $\Lambda + \bar{\Lambda}$  are reconstructed via the following fully hadronic decay channels:  $K_S^0 \rightarrow \pi^+ + \pi^-$  and  $\Lambda(\bar{\Lambda}) \rightarrow p(\bar{p}) + \pi^-(\pi^+)$  with branching ratios of 69.2% and 63.9% [67], respectively. The reconstruction is performed, as shown in Tab. 2, by identifying the candidates of secondary vertices, denoted as  $V^0$ s, from which two oppositely-charged decay products originate. Such candidates are obtained during data processing by looking for characteristic V-shaped decay topology among reconstructed tracks.

The daughter tracks were reconstructed within  $|\eta| < 0.8$ , while the criteria on the number of TPC space points, the number of crossed TPC padrows, and the percentage of the expected TPC space points used to reconstruct a track are identical to those applied for primary particles. In addition, the minimum DCA of daughter tracks to the primary vertex is 0.1 cm. Furthermore, the maximum DCA of daughter tracks to the secondary vertex is 0.5 cm to ensure that they are products of the same decay. To suppress the combinatorial background, PID is applied for the daughter particles in the whole  $p_T$  region by requiring the particle to be within  $3\sigma_{\text{TPC}}$  for a given species hypothesis.

To reject secondary vertices arising from decays into more than two particles, the cosine of the pointing angle,  $\theta_p$ , is required to be larger than 0.998. This angle is defined as the angle between the momentum vector of the  $V^0$  candidate assessed at its decay vertex and the line connecting the  $V^0$  decay vertex to the primary vertex and has to be close to 1 as a result of momentum conservation. In addition, only the candidates reconstructed between 5 and 100 cm from the nominal primary vertex in radial direction are accepted. The lower value is chosen to avoid any bias from the efficiency loss when secondary tracks are being wrongly matched to clusters in the first layer of the ITS. To assess the systematic uncertainty related to the contamination from  $\Lambda + \bar{\Lambda}$  and electron-positron pairs coming from  $\gamma$ -conversions to the  $K_S^0$  sample, a selection in the Armenteros-Podolanski variables [68] is applied for the  $K_S^0$  candidates, rejecting ones with  $q \leq 0.2|\alpha|$ . Here  $q$  is the momentum projection of the positively charged daughter track in the plane perpendicular to the  $V^0$  momentum and  $\alpha = (p_L^+ - p_L^-)/(p_L^+ + p_L^-)$  with  $p_L^\pm$  the projection of the positive or negative daughter tracks' momentum onto the momentum of the  $V^0$ .

The reconstruction of  $\phi$  meson candidates is done via the hadronic decay channel:  $\phi \rightarrow K^+ + K^-$  with a branching ratio of 48.9% [67]. The  $\phi$  meson candidates were reconstructed from the charged tracks passing all criteria for charged kaons, listed in Table 1. Kaon daughters are identified by utilising Bayesian PID approach [69] with a minimum probability threshold of 85% using TPC and TOF detectors. Additionally, to reduce combinatorial background of  $\phi$  candidates, a track is identified as kaon if it has the highest probability among all considered species ( $e, \mu, \pi^\pm, K^\pm, p + \bar{p}$ ). The vector sum of all possible pairs of charged kaons are called  $\phi$  candidates. The invariant mass distribution ( $M_{\text{inv}}^{K^+K^-}$ ) of  $\phi$  candidates is then obtained in various  $p_T$  intervals by subtracting a combinatorial background yield from the candidate yield. This combinatorial background yield is estimated from like-sign kaon pairs (unphysical  $\phi$  state with total charge of  $\pm 2$ ) normalised to the candidate yield.



## 4 Analysis method

In this article the  $p_T$ -differential non-linear flow modes are calculated according to Eqs. 12-15. Each event is divided into two subevents “A” and “B”, covering the ranges  $-0.8 < \eta < 0.0$  and  $0.0 < \eta < 0.8$ , respectively. Thus  $v_{n,mk}(p_T)$  is a weighted average of  $v_{n,mk}^A(p_T)$  and  $v_{n,mk}^B(p_T)$ . The measured  $v_{n,mk}^{A(B)}$  coefficients are calculated using  $d_{n,mk}^{A(B)}(p_T)$  and  $c_{mkmk}$  multi-particle correlators:

$$d_{n,mk}(p_T) = \langle \langle v_n(p_T) v_m v_k \rangle \rangle, \quad (10)$$

$$c_{mkmk} = \langle \langle v_m^2 v_k^2 \rangle \rangle. \quad (11)$$

These correlators are calculated using the Generic Framework introduced in [70], which allows precise non-uniform acceptance and efficiency corrections. In this analysis,  $d_{n,mk}^{A(B)}(p_T)$  is measured by selecting the identified hadrons (POIs) from subevent “A”(“B”) and the reference particles from subevent “B”(“A”) and  $c_{mkmk}$  by selecting half of the reference particles from subevent “A” and the other half from “B”. Thus, Eqs.6 to 9 for  $v_{n,mk}^A(p_T)$  translate to

$$v_{4,22}^A(p_T) = \frac{d_{4,22}^A(p_T)}{\sqrt{c_{2222}}} = \frac{\langle \langle \cos(4\phi_1^A(p_T) - 2\phi_2^B - 2\phi_3^B) \rangle \rangle}{\sqrt{\langle \langle \cos(2\phi_1^A + 2\phi_2^A - 2\phi_3^B - 2\phi_4^B) \rangle \rangle}}, \quad (12)$$

$$v_{5,32}^A(p_T) = \frac{d_{5,32}^A(p_T)}{\sqrt{c_{3232}}} = \frac{\langle \langle \cos(5\phi_1^A(p_T) - 3\phi_3^B - 2\phi_2^B) \rangle \rangle}{\sqrt{\langle \langle \cos(3\phi_1^A + 2\phi_2^A - 3\phi_3^B - 2\phi_4^B) \rangle \rangle}}, \quad (13)$$

$$v_{6,33}^A(p_T) = \frac{d_{6,33}^A(p_T)}{\sqrt{c_{3333}}} = \frac{\langle \langle \cos(6\phi_1^A(p_T) - 3\phi_2^B - 3\phi_3^B) \rangle \rangle}{\sqrt{\langle \langle \cos(3\phi_1^A + 3\phi_2^A - 3\phi_3^B - 3\phi_4^B) \rangle \rangle}}, \quad (14)$$

$$v_{6,222}^A(p_T) = \frac{d_{6,222}^A(p_T)}{\sqrt{c_{222222}}} = \frac{\langle \langle \cos(6\phi_1^A(p_T) - 2\phi_2^B - 2\phi_3^B - 2\phi_4^B) \rangle \rangle}{\sqrt{\langle \langle \cos(2\phi_1^A + 2\phi_2^A + 2\phi_3^A - 2\phi_4^B - 2\phi_5^B - 2\phi_6^B) \rangle \rangle}}, \quad (15)$$

where  $\langle \langle \rangle \rangle$  denotes an average over all particles and events.

This multi-particle correlation technique by nature removes majority of non-flow correlations. In order to reduce non-flow contributions further, a non-zero gap was applied between the two pseudorapidity regions as well as selecting like-sign particles of interest and reference particles. These variations did not affect the results significantly but any variation was included in the final systematics in Tab. 3 .

For inclusive charged hadrons, i.e.  $\pi^\pm$ ,  $K^\pm$  and  $p + \bar{p}$ , the  $d_{n,mk}$  correlators are calculated on a track-by-track basis as a function of  $p_T$  per centrality percentile. For particle species reconstructed on statistical basis from decay products, i.e.  $K_S^0$ ,  $\Lambda + \bar{\Lambda}$  and  $\phi$  meson, the selected sample contains both signal and the combinatorial background. Therefore, for the aforementioned particle species, the  $d_{n,mk}$  correlators are measured as a function of invariant mass ( $M_{inv}$ ) and  $p_T$  per centrality percentile. The  $d_{n,mk}$  vs.  $M_{inv}$  method is based on the additivity of correlations and is a weighted sum of the  $d_{n,mk}^{sig}$  and  $d_{n,mk}^{bkg}$  according to

$$d_{n,mk}(M_{inv}) = \frac{N^{sig}}{N^{sig} + N^{bkg}}(M_{inv})d_{n,-m,-k}^{sig} + \frac{N^{bkg}}{N^{sig} + N^{bkg}}(M_{inv})d_{n,-m,-k}^{bkg}(M_{inv}), \quad (16)$$

where  $N^{\text{sig}}$  and  $N^{\text{bkg}}$  are signal and background yields obtained for each  $p_T$  interval and centrality percentile from fits to  $K_S^0$ ,  $\Lambda + \bar{\Lambda}$  and  $\phi$  meson invariant mass distributions. To obtain the  $p_T$ -differential yield of  $K_S^0$  and  $\Lambda + \bar{\Lambda}$  (which, together with background yields), are used for the signal extraction in Eq. 16, invariant mass distributions at various  $p_T$  intervals are parametrized as a sum of two Gaussian distribution and a third-order polynomial function. The latter is introduced to account for residual contamination (background yield) that are present in the  $K_S^0$  and  $\Lambda + \bar{\Lambda}$  signals after the topological and daughter track selections. The  $K_S^0$  and  $\Lambda + \bar{\Lambda}$  yields are extracted by integration of the Gaussian distribution. Similarly, to obtain the  $p_T$ -differential yield of  $\phi$ -mesons, the invariant mass distributions of the candidate yield is parametrized as a sum of a Breit-Wigner distribution and a third-order polynomial function, the latter introduced to account for residual contamination.

To extract  $d_{n,mk}^{\text{sig}}$ ,  $d_{n,mk}(M_{\text{inv}})$  is fitted together with the fit values from the invariant mass distribution and parametrising  $d_{n,mk}^{\text{bkg}}(M_{\text{inv}})$  with a first order polynomial function. Figure 1 illustrates this procedure for the  $\phi$ -meson, with the invariant mass distribution in the upper panel and the measurement of  $d_{4,22}(M_{\text{inv}})$  in the lower panel.

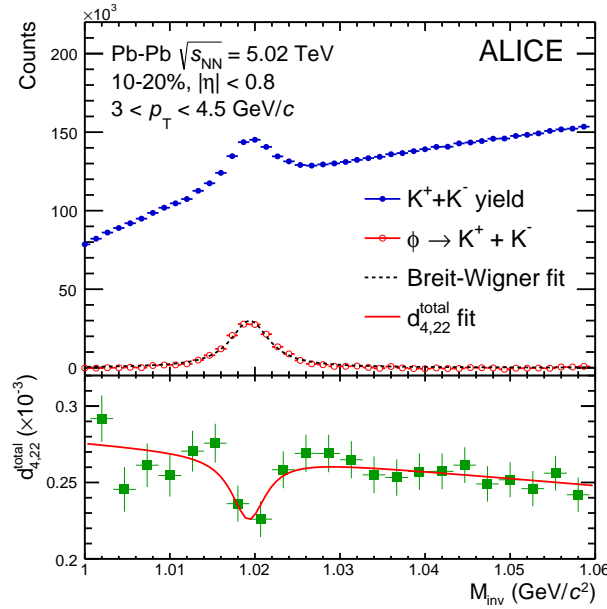


**Figure 1:** Reconstruction and  $d_{4,22}$  measurement of  $\phi$ -meson. Upper panel: extraction of  $N^{\text{sig}}$  and  $N^{\text{bkg}}$  by fitting the invariant mass ( $M_{\text{inv}}$ ) distribution for  $\phi$ -meson for  $3 < p_T < 4.5$  GeV/ $c$  at 10-20% centrality interval, lower panel: extraction of  $d_{4,22}^{\text{sig}}$  by fitting Eq. 16 to the invariant mass dependence of  $d_{4,22}$

## 5 Systematic uncertainties

The systematic uncertainties are estimated by varying the selection criteria for all particle species as well as topological reconstruction requirements for  $K_S^0$ ,  $\Lambda + \bar{\Lambda}$  and  $\phi$ . The contributions from different sources are extracted from the relative ratio of the  $p_T$ -differential  $v_{n,mk}$  between the default selection criteria described in Section 3 and their variations summarised in Tabs. 1 and 2. Each source with a statistically significant contribution, i.e.  $|x_1 - x_2| / \sqrt{(\sigma_1^2 \pm \sigma_2^2)} > 1$  (known as barlow check [71]) was fitted to create a smooth change along  $p_T$  and then the value of these fits were added in quadrature to form the final value of the systematic uncertainties on the non-linear flow modes. An overview of the magnitude of the relative systematic uncertainties per particle species is given in Tab. 3 for  $\pi^\pm$ ,  $K^\pm$  and  $p + \bar{p}$  and Tab. 4 for  $K_S^0$ ,  $\Lambda + \bar{\Lambda}$  and  $\phi$ -meson. Systematic uncertainties are grouped into five categories,

Selection requirement	Default	Variations
Primary $vx_z$	$\pm 10$ cm	$\pm 6$ cm, $\pm 8$ cm
Centrality estimator	V0M	CL0, CL1
Magnetic field polarity	both fields	++, --
pile-up rejection	strict	loose
Tracking mode	global (96)	hybrid (768)
Number of TPC space-points	70	60, 80, 90
$\chi^2$ per TPC space-point	4	3
DCA <sub>xy</sub> cm	$p_T$ dependant	0.2, 0.15 cm
DCA <sub>z</sub> cm	2 cm	0.2, 0.3 cm
PID method	$p_T$ -dependent	tight $p_T$ -dependent, Bayesian prob. >80%
POI vs. RFP charges	All	++, --
$\eta$ gap	0.0	0.4

**Table 1:** List of the selection criteria and the corresponding variations used for the estimation of the systematic uncertainties of  $\pi^\pm$ ,  $K^\pm$  and  $p + \bar{p}$

Selection requirements	Default	Variations
Reconstruction method ( $V^0$ finder)	offline	online
Decay vertex (radial position)	$5 < r < 100$ cm	$10 < r < 100$ cm
Cosine of pointing angle	$> 0.998$	$> 0.99$
Number of crossed TPC clusters	$> 70$	$> 90$
Number of TPC clusters used for PID	$> 70$	$> 90$
Number of findable TPC clusters	$> 1$	–
Ratio of crossed to findable TPC clusters	$> 0.8$	$> 1.0$
DCA decay products to primary vertex	$> 0.1$ cm	$> 0.3$ cm
DCA among daughters	$< 0.5$ cm	$< 0.3$ cm
Daughter $p_T$ acceptance	–	$> 0.2$ GeV/c
TPC PID on daughters	$< 3\sigma$	–
Armenteros-Podolanski ( $K_S^0$ )	$q > 0.2 \alpha $	–
Daughter $\eta$ acceptance	$ \eta  < 0.8$	–
Mother $\eta$ acceptance	$ \eta  < 0.8$	–
Competing inv. mass rejection ( $K_S^0$ )	$< 5$ MeV <sup>2</sup>	–
Competing inv. mass rejection ( $\Lambda + \bar{\Lambda}$ )	$< 10$ MeV <sup>2</sup>	–

**Table 2:** List of topological reconstruction requirements and cuts applied on  $V^0$  candidates including variations for systematical uncertainty study where applicable.

i.e. event selection, tracking, particle identification, topological cuts and non-flow contribution and are described below.

The effects of event selection criteria on the measurements are studied by: (i) varying the primary vertex position along the beam axis ( $z_{vtx}$ ) from a nominal  $\pm 10$  cm to  $\pm 8$  cm and  $\pm 6$  cm; (ii) changing the centrality estimator from the signal amplitudes in the V0 scintillator detectors to the multiplicity of TPC tracks or the number of SPD clusters; (iii) analysing events recorded for different magnetic field polarities independently; (iv) not rejecting events with tracks caused by pileup.

Systematic uncertainties induced by the selection criteria imposed at the track level were investigated by: (i) changing the tracking from global mode where combined track information from both TPC and ITS detectors are used to hybrid mode in which track parameters from TPC are used if the algorithm is unable to match the track reconstructed in the TPC with associated ITS clusters; (ii) increasing the number of TPC space points from 70 up to 100 and (iii) decreasing the value of the  $\chi^2$  per TPC space point per degree of freedom from 4 to 2; (iv) varying the selection criteria on both the longitudinal and transverse components of the DCA to estimate the impact of secondary particles from a strict  $p_T$ -dependent cut to 0.15 cm and 2 cm to 0.2 cm, respectively.

Systematic uncertainties associated with the particle identification procedure were studied by varying the PID method from a  $p_T$ -dependent one described in 3.2 to a stricter version where the purity increases to 95% ( $\pi^\pm$ ), 80% ( $K^\pm$ ) and 80% ( $p + \bar{p}$ ) across the entire  $p_T$  range of study. The second approach used relied on the Bayesian method with a probability of at least 80% which gives an increase in purity to 97% ( $\pi^\pm$ ), 87% ( $K^\pm$ ) and 90% ( $p + \bar{p}$ ) across the entire  $p_T$  range of study.

In addition, the non-flow contribution is studied by (i) selecting like sign pairs of particles of interest and reference particles to decrease the effect from decay of resonance particles; (ii) applying pseudorapidity gaps between the two subevents from  $|\Delta\eta| > 0.0$  to  $|\Delta\eta| > 0.4$ .

The topological cuts were also varied to account for the  $V^0$  and  $\phi$ -meson reconstruction. The default  $V^0$  finding method is described in Sec. 3.3. These selection criteria are varied by (i) changing the reconstruction method for  $V^0$  particles from offline to online; (ii) varying the minimum radial distance to the primary vertex at which the  $V^0$  can be produced from 5 cm to 10 cm; (iii) changing the minimum value of cosine of pointing angle from 0.998 to 0.99; (iv) varying the minimum number of TPC space points crossed by the  $V^0$  daughter tracks from 70 to 90; (v) changing the requirement on the minimum number of TPC space points that are used in the reconstruction of the  $V^0$  daughter tracks from 70 to 90; (vi) requesting a minimum ratio of crossed to findable TPC clusters from 0.8 to 1.0; (vii) changing the minimum DCA of the  $V^0$  daughter tracks to the primary vertex from 0.1 cm to 0.3 cm; (viii) changing the maximum DCA of the  $V^0$  daughter tracks to the secondary vertex from 0.5 cm to 0.3 cm; (ix) requiring a minimum  $p_T$  of the  $V^0$  daughter tracks of 0.2 GeV/c.

The contributions from each source were added in quadrature to form the total systematic uncertainties. This will be represented in all plots of this article as a box around each data point while the statistical uncertainty will be shown by the error bars.

Error source	$v_{4,22}$			$v_{5,32}$			$v_{6,33}$			$v_{6,222}$		
	$\pi^\pm$	$K^\pm$	$p + \bar{p}$	$\pi^\pm$	$K^\pm$	$p + \bar{p}$	$\pi^\pm$	$K^\pm$	$p + \bar{p}$	$\pi^\pm$	$K^\pm$	$p + \bar{p}$
Primary $z_{vtx}$	0-2%	1-3%	0-3%	0-3%	1-3%	1-4%	3-5%	2-5%	3-5%	2-7%	2-7%	4-7%
Centrality estimator	0-4%	1-4%	1-5%	0-4%	1-3%	2-4%	4-10%	4-10%	5-10%	3-10%	5-10%	4-10%
Magnetic field polarity	0-2%	0-3%	0-3%	0-4%	0-5%	0-5%	0-10%	0-10%	0-10%	0-10%	0-10%	0-10%
Pileup rejection	0-4%	0-4%	0-4%	0-5%	1-5%	0-5%	5-7%	5-10%	5-8%	4-10%	4-10%	2-10%
Tracking mode	1-4%	1-5%	1-4%	2-6%	3-5%	2-8%	0-8%	0-7%	3-8%	1-10%	4-10%	2-10%
Number of TPC space-points	1-2%	0-2%	0-2%	0-3%	1-3%	1-3%	4-8%	3-8%	3-8%	2-8%	4-8%	4-8%
$\chi^2$ per TPC space-point	0-2%	1-2%	1-3%	1-3%	1-3%	2-4%	3-5%	3-6%	3-6%	2-6%	4-7%	4-7%
DCAxy	0-2%	0-2%	1-3%	0-3%	1-3%	1-3%	2-7%	2-8%	4-8%	2-8%	4-8%	3-8%
DCAz	0-3%	0-2%	1-2%	1-2%	1-3%	2-3%	3-7%	3-7%	5-7%	2-7%	4-8%	2-8%
Particle identification	1-5%	1-5%	1-3%	1-5%	2-5%	1-5%	5-10%	5-10%	6-12%	4-12%	6-15%	4-15%
POI vs. RFP charges	0-2%	0-3%	2-3%	0-4%	0-4%	2-4%	0-4%	0-6%	0-6%	0%	0%	0%
$\eta$ gap	1-3%	1-4%	1-2%	1-4%	1-4%	1-5%	0-5%	0-5%	0-5%	0%	0%	0%

**Table 3:** List of the maximum systematic uncertainties from each individual source for  $v_{n,mk}$  of  $\pi^\pm$ ,  $K^\pm$  and  $p + \bar{p}$ . The uncertainties depend on the transverse momenta and centrality interval. Hence here ~~maximum and~~ maximum values are listed in ranges.

Error source	$v_{4,22}$			$v_{5,32}$		$v_{6,33}$	
	$K_S^0$	$\Lambda + \bar{\Lambda}$	$\phi$	$K_S^0$	$\Lambda + \bar{\Lambda}$	$K_S^0$	$\Lambda + \bar{\Lambda}$
Primary $z_{\text{vtx}}$	0%	0-2%	1%	0%	0-3%	0%	1-3%
Tracking mode	-	-	2%	-	-	-	-
Number of TPC space-points	0-3%	1-2%	2%	0%	2%	0%	2%
Particle identification	-	-	4-6%	-	-	-	-
Reconstruction method ( $V^0$ finder)	3-5%	2-3%	N/A	5%	1%	5%	1%
Decay radius	3-5%	1-3%	N/A	5-6%	0-2%	5%	2%
Ratio of crossed to findable TPC clusters	0-2%	0-3%	N/A	0%	1-2%	0%	3%
DCA decay products to primary vertex	2-5%	2-4%	N/A	4-5%	2-3%	5%	2-3%
DCA between decay products	0-3%	1-2%	N/A	0-4%	0-4%	0%	0-4%
Pointing angle $\cos(\theta_p)$	3-4%	0-2%	N/A	3-4%	0-3%	3%	1%
Minimum $p_T$ of daughter tracks	1-3%	0-1%	N/A	2-3%	2-3%	0%	0-3%

**Table 4:** List of the maximum systematic uncertainties from each individual source for  $v_{n,mk}$  of  $K_S^0$ ,  $\Lambda + \bar{\Lambda}$  and  $\phi$ -meson. The uncertainties depend on the transverse momenta and centrality interval. Hence here maximum and minimum values are listed. "N/A" indicates that a certain check was not applicable to the given particle of interest. If a source was checked and proved to be of negligible effect, the field is marked with "-".

## 6 Results and discussion

In this section, the results for the  $p_T$ -dependent non-linear flow modes  $v_{4,22}$ ,  $v_{5,32}$ ,  $v_{6,33}$  and  $v_{6,222}$  of identified particles are presented for various centrality intervals in Pb–Pb collisions at  $\sqrt{s_{\text{NN}}} = 5.02$  TeV. We first present the centrality and  $p_T$  dependence of  $v_{n,mk}$  in Sec. 6.1. The scaling properties of non-linear flow modes are also discussed in this section. Comparisons to two model calculations are shown in Sec. 6.3. Note that the same data are used in different representations to highlight the physics implications of the measurements in each section.

### 6.1 Centrality and $p_T$ dependence of non-linear flow modes

Higher order flow coefficients ( $n > 3$ ) are mainly generated by inhomogeneities in the initial density profile and the collision geometry as well as the non-linear hydrodynamic response of the system. Figure 2 presents the non-linear term for the fourth order flow coefficient, i.e.  $v_{4,22}(p_T)$ , of  $\pi^\pm$ ,  $K^\pm$ ,  $K_S^0$ ,  $p + \bar{p}$ ,  $\Lambda + \bar{\Lambda}$  and  $\phi$ -meson for a wide range of centrality intervals, i.e. 0-60%. For the  $\phi$ -meson, the results are reported in the 10-50% centrality interval, where  $v_{4,22}$  can be measured accurately. The magnitude of  $v_{4,22}$  rises steeply with increasing centrality interval from 0-5% to 40-50% for all particle species. This increase is expected as  $v_{4,22}$  measures the contribution of the second order eccentricity,  $\epsilon_2$ , in  $v_4$  which increases for peripheral collisions [8]. For more peripheral collisions (i.e. 50-60%), the magnitude of  $v_{4,22}$  is smaller than in the previous centrality intervals for all particle species. This effect that was observed also in  $v_n$  measurements is probably due to the shorter lifetime of the produced system in more peripheral collisions, which prevents  $v_{4,22}$  from developing further.

Figure 3 presents the non-linear term for the fifth order flow coefficient, i.e.  $v_{5,32}(p_T)$ , of  $\pi^\pm$ ,  $K^\pm$ ,  $K_S^0$ ,  $p + \bar{p}$ , and  $\Lambda + \bar{\Lambda}$  for the same range of centrality intervals, i.e. 0-60%. Statistical precision limits extending the measurements of non-linear flow modes of  $\phi$ -meson for  $n > 4$ . The measurements show a significant increase in the magnitude of this non-linear flow mode with increasing centrality percentile. This is due to the fact that  $v_{5,32}(p_T)$  has a contribution from both  $\epsilon_2$  and  $\epsilon_3$ . It is shown in MC studies that both  $\epsilon_2$  and  $\epsilon_3$  increase for peripheral collisions [8]. Although, this increase is less pronounced for  $\epsilon_3$ .

Figure 4 and 5 present the non-linear terms for the sixth order flow coefficient, i.e.  $v_{6,33}(p_T)$  for  $\pi^\pm$ ,  $K^\pm$ ,  $K_S^0$ ,  $p + \bar{p}$  and  $\Lambda + \bar{\Lambda}$  and at 0-50% centrality intervals and  $v_{6,222}(p_T)$  for  $\pi^\pm$ ,  $K^\pm$ ,  $p + \bar{p}$  at 0-60% centrality intervals. As expected, measurements of  $v_{6,222}(p_T)$  show an increase in the magnitude of this non-linear flow mode with increasing centrality percentile, whereas,  $v_{6,33}(p_T)$  presents little to no dependence on centrality.

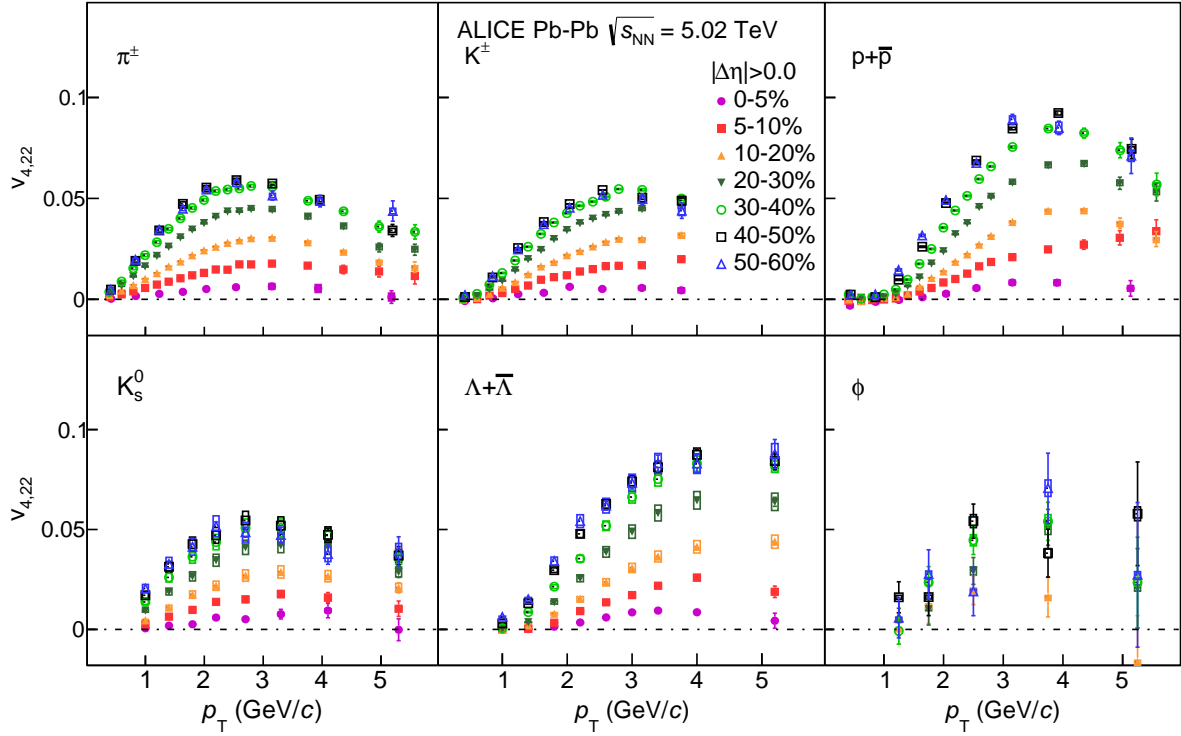


**Figure 2:** The  $p_T$ -differential  $v_{4,22}$  for different centrality intervals of Pb–Pb collisions at  $\sqrt{s_{NN}} = 5.02$  TeV grouped by particle species.

In Fig. 6 the same data points are grouped by centrality interval to highlight how  $v_{4,22}$  develops for a given centrality for various particle species as a function of  $p_T$ . A clear mass ordering can be seen in the low  $p_T$  region (i.e.  $p_T < 2.5$  GeV/c) at all collision centralities. This mass dependence ordering arises from the interplay between the anisotropic flow and radial flow. Radial flow creates a depletion in the particle spectra at lower  $p_T$  values which leads to lower  $v_{4,22}$  for heavier particles [51, 52, 72].

Similarly, Figs. 7, 8 and 9 show the  $p_T$ -differential  $v_{5,32}$ ,  $v_{6,33}$  and  $v_{6,222}$  respectively, of different particle species for each centrality interval. A clear mass ordering is seen in the low  $p_T$  region, (i.e.  $p_T < 2.5$  GeV/c), for  $v_{5,32}(p_T)$ ,  $v_{6,33}(p_T)$  and  $v_{6,222}(p_T)$ , which similarly arises from the interplay between the non-linear response of the system and radial flow.

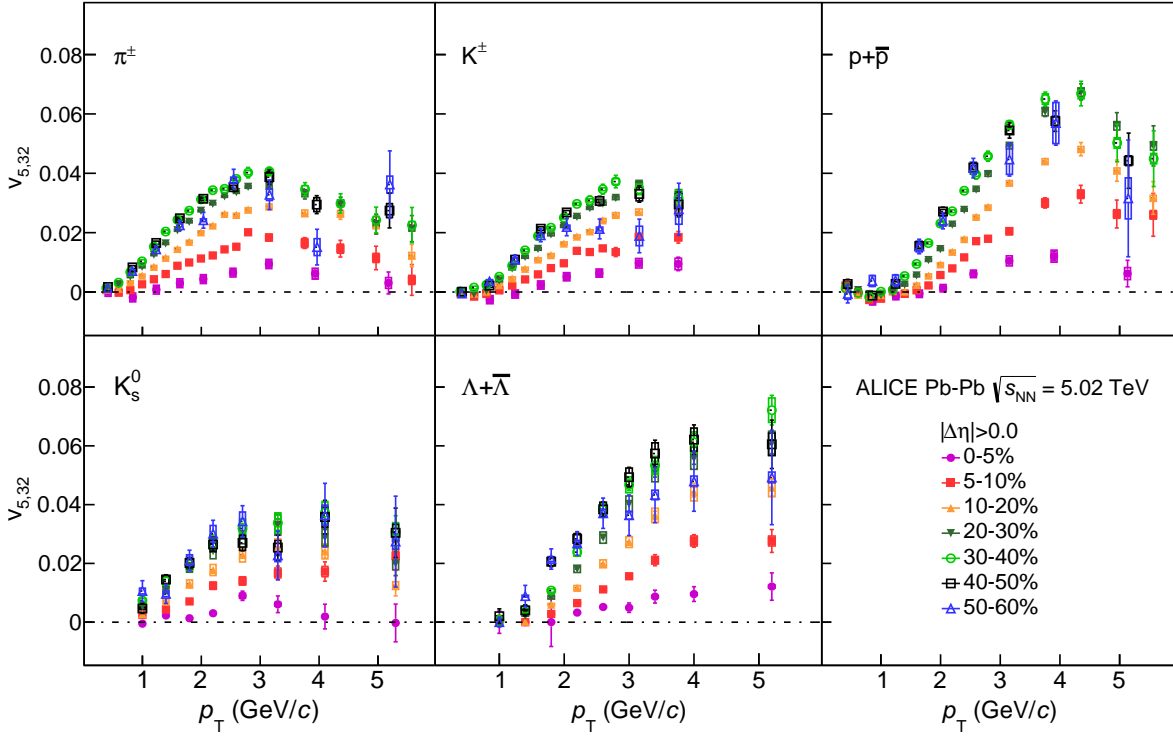


**Figure 3:** The  $p_T$ -differential  $v_{5,32}$  for different centrality intervals of Pb–Pb collisions at  $\sqrt{s_{NN}} = 5.02$  TeV grouped by particle species.

In addition, in the intermediate  $p_T$  region (for  $p_T > 2.5$  GeV/c) the data points of Figs. 6-9 exhibit a particle type grouping. In particular, mesons ( $\pi^\pm$ ,  $K^\pm$ ,  $K_S^0$  and  $\phi$ ) and baryons ( $p + \bar{p}$  and  $\Lambda + \bar{\Lambda}$ ) group based on their type with  $v_{n,mk}$  of baryons having a larger magnitude. This particle type grouping was previously ~~seen~~ observed in the anisotropic flow measurements of various particle species [13–16, 37, 38, 40]. This suggests that flow develops at the partonic stage and if so, combining two or three quarks to form hadronic states might result into hadrons inheriting the transverse momentum and subsequently,  $v_n$  of their constituents. As a next step it was suggested to use a form of number of constituent quark (NCQ) scaling in which both flow coefficients and  $p_T$  were scaled by the number of constituent quarks ( $n_q$ ). This scaling, worked initially at RHIC energies, although later measurements revealed sizeable deviations from a perfect scaling [13–16]. ALICE measurements showed that the NCQ scaling at LHC energies holds at ~~best~~ at an approximate level of 20% for  $v_n$  [37, 38, 40]. Various theoretical ideas were created to address the origin of possible scaling by requiring quark coalescence to be the dominant particle production mechanism in the intermediate  $p_T$  region, where the hydrodynamic evolution of the fireball is not the driving force behind the development of anisotropic flow [54, 55].

Figures 10, 11, 12 and 13 present  $v_{4,22}$ ,  $v_{5,32}$ ,  $v_{6,33}$  and  $v_{6,222}$  respectively, scaled by the inverse of number of constituent quarks ( $n_q$ ) as a function of  $p_T/n_q$  for  $\pi^\pm$ ,  $K^\pm$ ,  $K_S^0$ ,  $p + \bar{p}$ ,  $\Lambda + \bar{\Lambda}$  and  $\phi$ -meson grouped in different centrality intervals. The scaling is consistent with the observations reported for higher order total flow coefficients [40]. Similarly, for non-linear flow modes this scaling hold at ~~best~~ at an approximate level ( $\pm 20\%$ ).

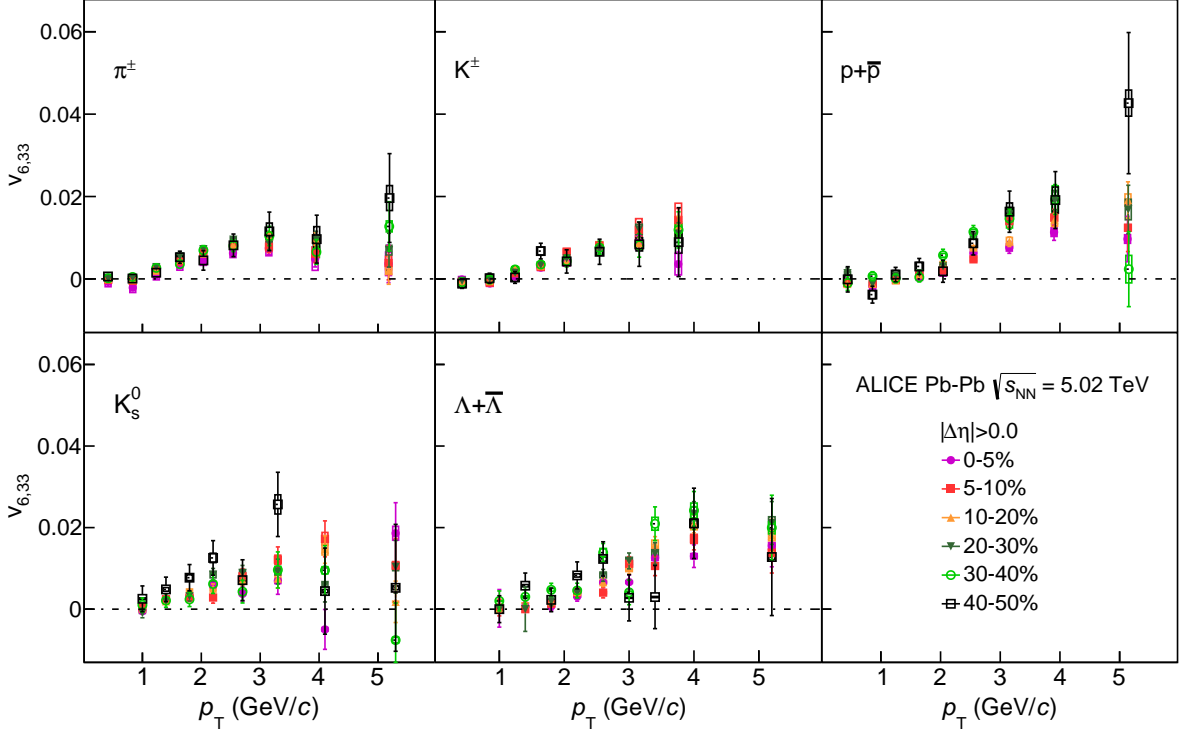


**Figure 4:** The  $p_T$ -differential  $v_{6,33}$  for different centrality intervals of Pb–Pb collisions at  $\sqrt{s_{NN}} = 5.02$  TeV grouped by particle species.

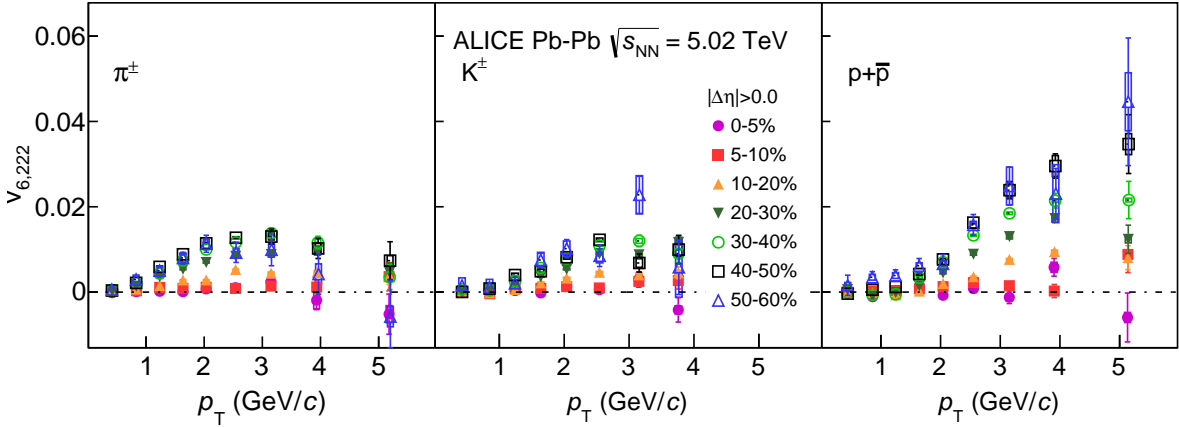


**Figure 5:** The  $p_T$ -differential  $v_{6,222}$  for different centrality intervals of Pb–Pb collisions at  $\sqrt{s_{NN}} = 5.02$  TeV grouped by particle species.

## 6.2 Comparison with models

Measurements of total flow coefficients at RHIC and the LHC are described well by hydrodynamic calculations [73–75]. A recent comparison between total flow measurements at ALICE [40] and two hydrodynamic calculations from [75] shed new light on the initial conditions and the transport proper-



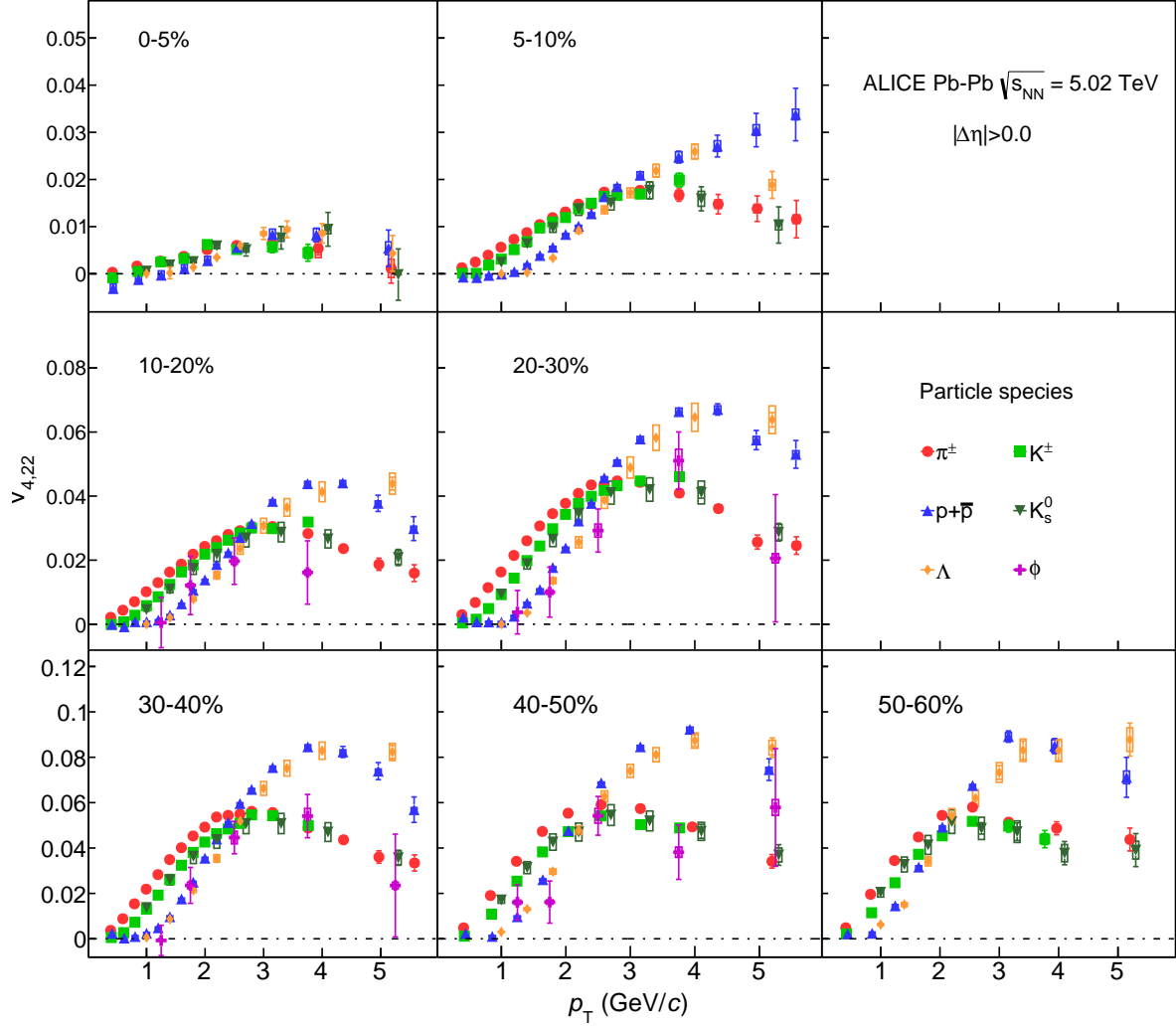


**Figure 6:** The  $p_T$ -differential  $v_{4,22}$  for different particle species grouped into different centrality intervals of Pb–Pb collisions  $\sqrt{s_{NN}} = 5.02$  TeV

ties of the created system in Pb–Pb collisions. Both calculations are based on iEBE-VISHNU [76], an event-by-event version of the VISHNU hybrid model [77] coupling 2 + 1 dimensional viscous hydrodynamics (VISH2+1) [78] to a hadronic cascade model (UrQMD). The initial conditions used for these calculations are described by AMPT [79] and TRENTo [80], both with  $\tau_0=0.6$  fm/c and  $T_{sw}=148$  MeV [81]. These values are obtained from the global bayesian analysis [81]. For AMPT initial conditions, constant values of specific shear viscosity ( $\eta/s = 0.08$ , the lower limit conjectured by AdS/CFT) and bulk viscosity ( $\zeta/s = 0$ ) are utilised, and TRENTo [80] initial conditions incorporates a temperature dependent specific shear and bulk viscosity extracted from the global bayesian analysis.<sup>1</sup> The comparison between the total flow measurements and these two calculations illustrates a qualitative agreement. This agreement between the data and the models depends on the particle species, transverse momentum range and centrality percentile and overall the AMPT model reproduces these measurements more accurately than TRENTo model [40].

<sup>1</sup>For simplicity in the rest of this article the model with AMPT initial conditions,  $\eta/s = 0.08$  and  $\zeta/s = 0$  is referred to as AMPT and the model with TRENTo initial conditions,  $\eta/s(T)$  and  $\zeta/s(T)$  is referred to as TRENTo.

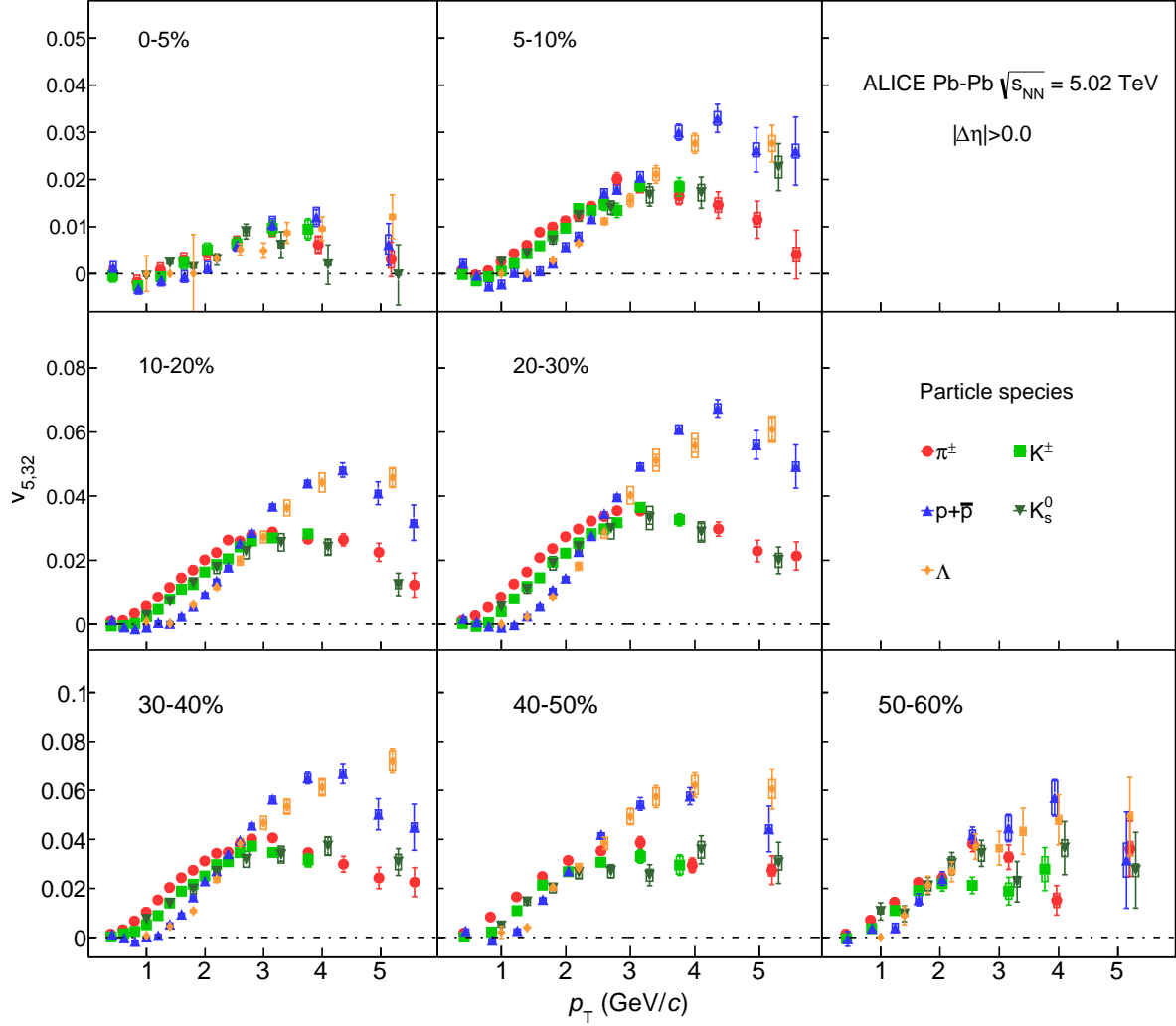


**Figure 7:** The  $p_T$ -differential  $v_{5,32}$  for different particle species grouped into different centrality intervals of Pb–Pb collisions  $\sqrt{s_{NN}} = 5.02$  TeV

Recently, it was shown that the  $p_T$ -integrated non-linear flow modes are good observables to constrain the initial conditions and transport properties of the system [48]. To further constrain the initial conditions and transport properties of the system and test the validity of these hydrodynamic models a comparison is performed between the measured  $p_T$ -dependent non-linear flow modes for  $\pi^\pm$ ,  $K^\pm$  and  $p + \bar{p}$  with two hydrodynamical calculations from [75] as were used in comparison to the anisotropic flow measurements [40].

Figures 14, 15, 16 and 17 present the comparison between the measurements (data points in the plots) and both models for the  $p_T$ -differential  $v_{4,22}$ ,  $v_{5,32}$ ,  $v_{6,33}$  and  $v_{6,222}$ , respectively, for  $\pi^\pm$ ,  $K^\pm$  and  $p + \bar{p}$  at 0-10% up to 50-60% centrality interval (40-50% centrality interval for  $v_{6,33}$ ) of Pb–Pb collisions at  $\sqrt{s_{NN}} = 5.02$  TeV. The solid bands show the AMPT model and the hatched bands represent the TRENTo calculations. The bottom panels in each plot in Figs. 14, 15, 16 and 17 present the difference between the models and the measurement.

Both TRENTo and AMPT models produce a mass ordering in  $p_T < 2.5$  GeV/c for all non-linear flow modes. In particular, the comparison between the models and the measurements of  $v_{4,22}$  reveals that

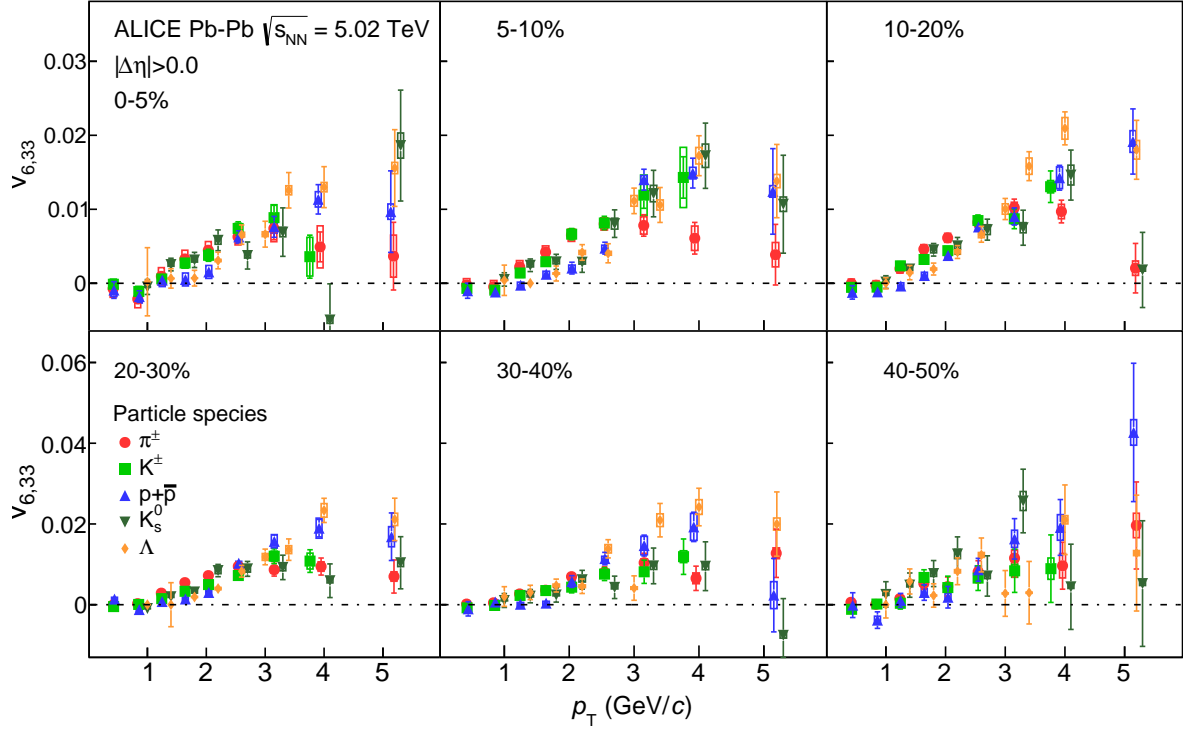


**Figure 8:** The  $p_T$ -differential  $v_{6,33}$  for different particle species grouped into different centrality intervals of Pb–Pb collisions  $\sqrt{s_{NN}} = 5.02$  TeV

in more central collisions TRENTo reproduces the data very well from 0-10% up to 30-40% centrality interval and fails to reproduce the measurements for 40-50% and 50-60% whereas AMPT overestimates the measurements from 0-10% up to 30-40% centrality interval. For more peripheral collisions AMPT reproduces the  $K^\pm$  and  $p + \bar{p}$  measurements and underestimates the  $\pi^\pm$  measurements. For  $v_{5,32}$ , the comparisons seem slightly different where TRENTo predictions overestimate the measurements for all centrality intervals. While AMPT seemingly reproduces the data better; it slightly overestimates the measurements from 0-10% to 20-30% centrality interval and ~~slightly~~ underestimates the measurements for more peripheral collisions. For  $v_{6,33}$ , both models reproduce the data at 0-10% centrality interval. For 10-20% up to 30-40% centrality interval, AMPT reproduces the data while TRENTo slightly overestimates the measurements. Finally, comparisons with  $v_{6,222}$  shows an agreement between both models and the data at 0-10% up to 30-40% centrality intervals. ~~All in all, comparing this effort to the data-model comparison for anisotropic flow coefficients [40] shows that~~

These two models have been already utilised to reproduce the  $p_T$ -differential  $v_n$  measurements for identified particles [40]. In order to compare the performance of these two models in  $v_n$  and  $v_{n,mk}$  measurements, the relative ratios have been obtained between each model and the measurements. Tables 5 and 6 summarize these relative ratios for non-linear modes are more sensitive to the initial conditions and transport properties. However, similar to model-data comparisons for flow modes and anisotropic flow, neither of respectively. The ranges in the tables present the minimum and maximum value of a pol0 fit to the relative ratios obtained from most-central to mid-peripheral collisions. These values should be taken with caution as the non-linear flow modes have smaller magnitude and any discrepancy between the models and the data gets magnified in the ratios. Comparison between the two tables shows that the AMPT IC reproduces  $v_{4,22}$  with  $\sim 20\%$  higher discrepancy on average compared to  $v_4$ , while, TRENTo IC performs better in  $v_{4,22}$  compared to  $v_4$  with  $\sim 7\%$ .

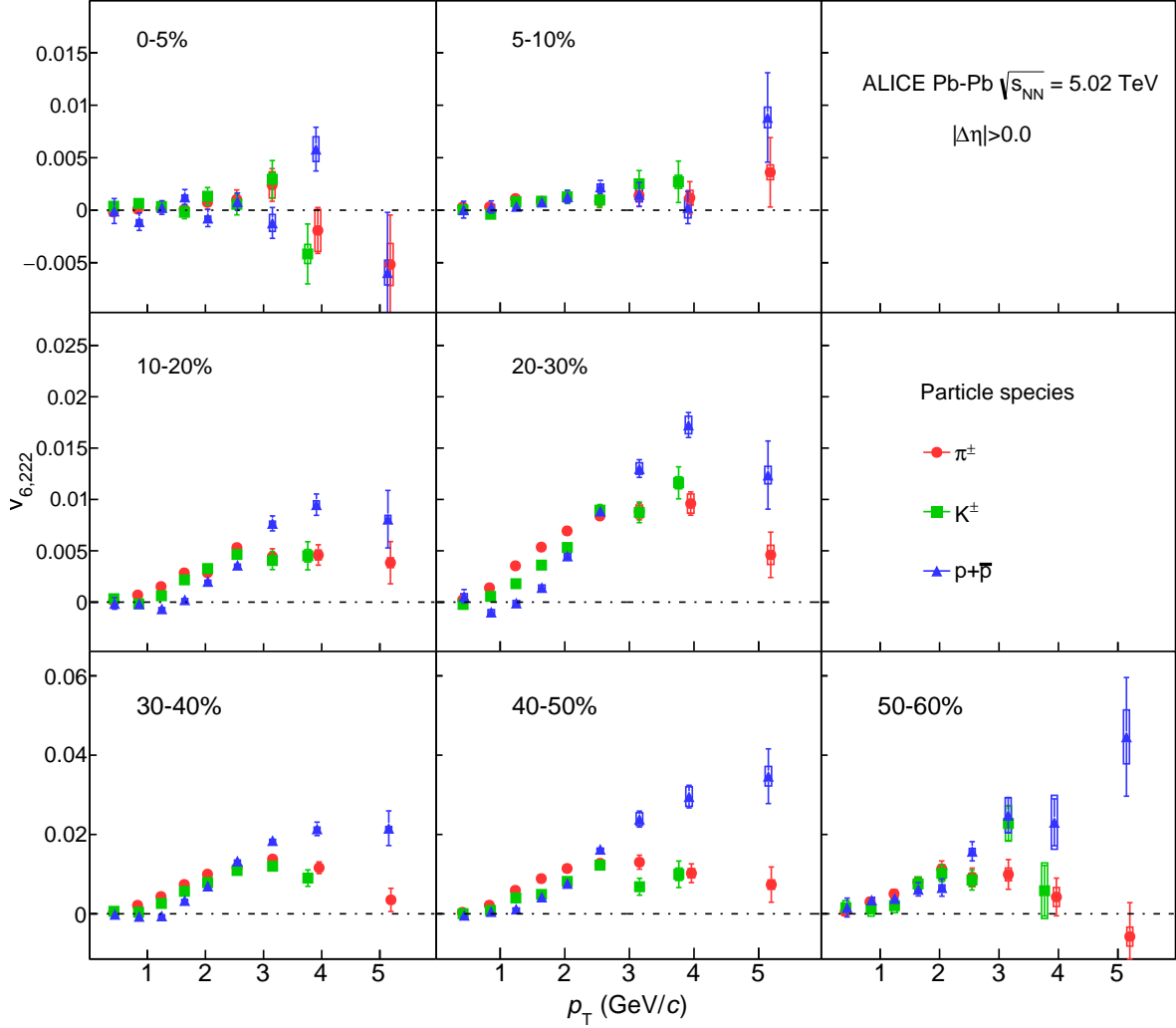


**Figure 9:** The  $p_T$ -differential  $v_{6,222}$  for different particle species grouped into different centrality intervals of Pb–Pb collisions  $\sqrt{s_{NN}} = 5.02$  TeV

All in all, this study shows lower discrepancy between the model calculations and anisotropic flow wrt. that of non-linear flow modes, indicating a larger sensitivity to the models can reproduce the data for all centrality intervals and particle species. As a result, in order to constrain the values of transport properties and the initial conditions of the system and transport properties in non-linear flow modes. As a result, it is necessary to tune the input parameters of hydrodynamic models using these measurements the non-linear flow measurements, to constrain the values of transport properties and the initial conditions of the system.

Error source	$v_{4,22}$			$v_{5,32}$			$v_{6,33}$			$v_{6,222}$		
	$\pi^\pm$	$K^\pm$	$p + \bar{p}$	$\pi^\pm$	$K^\pm$	$p + \bar{p}$	$\pi^\pm$	$K^\pm$	$p + \bar{p}$	$\pi^\pm$	$K^\pm$	$p + \bar{p}$
AMPT IC	5-30%	2-30%	3-30%	3-28%	5-29%	1-65%	0-46%	0-46%	0-97%	6-52%	0-80%	0-118%
TRENT0 IC	0-30%	4-33%	0-21%	24-49%	33-97%	12-58%	0-43%	0-46%	0-95%	0-20%	0-34%	0-78%

**Table 5:** List of minimum and maximum value of the fit to relative ratios between the data and each model for  $v_{n,mk}$  of  $\pi^\pm$ ,  $K^\pm$  and  $p + \bar{p}$ . The minimum and maximum are obtained from 0-10% up to 50-60% (40-50% for  $v_{6,33}$ ) centrality intervals.

The differential  $v_{5,32}$  for different particle species in 10-20% up to 50-60% centrality intervals of

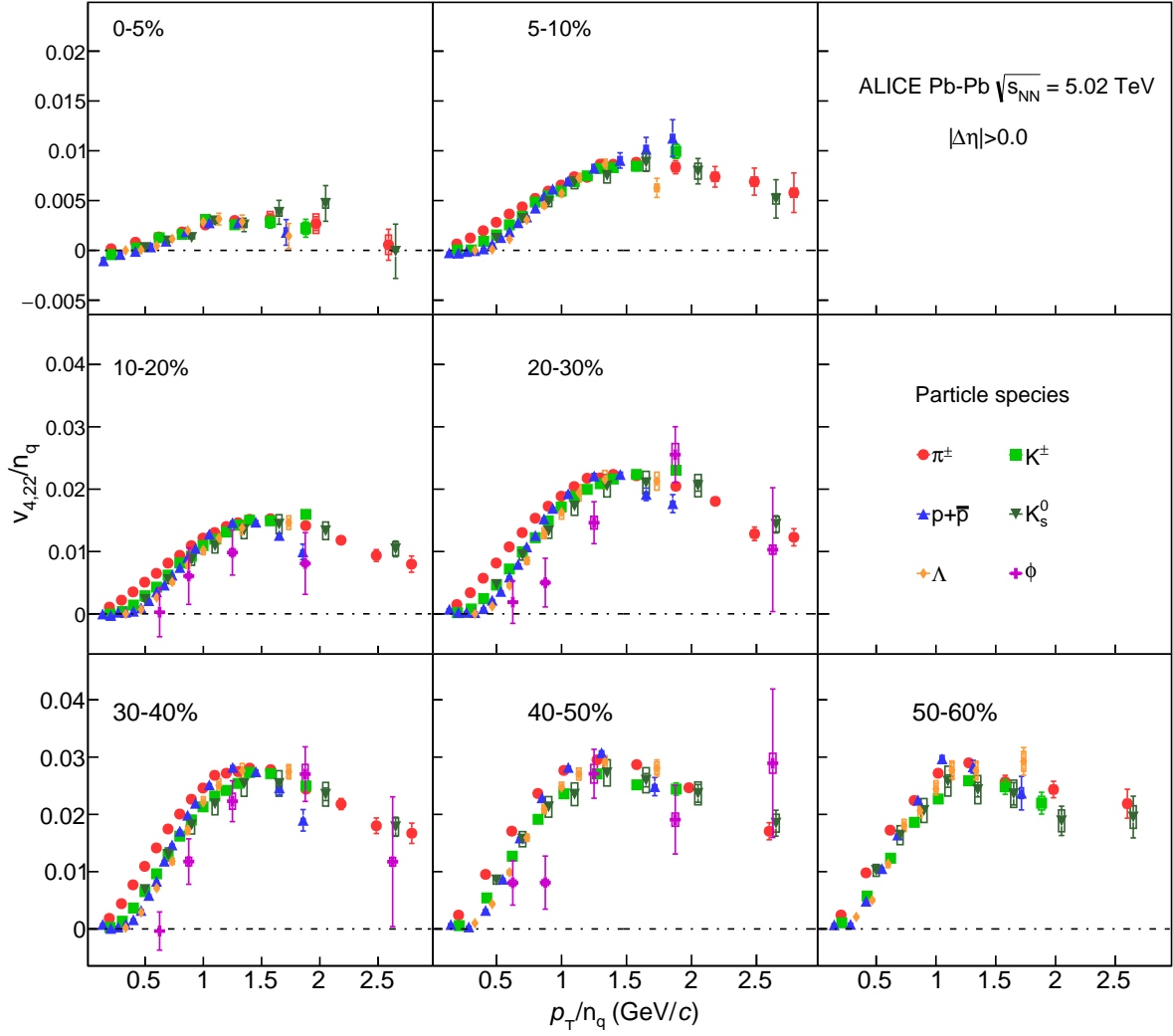


**Figure 10:** The  $p_T/n_q$ -dependence of  $v_{4,22}/n_q$  for different particle species grouped into different centrality intervals of Pb–Pb collisions  $\sqrt{s_{NN}} = 5.02$  TeV

Error source	$v_2$			$v_3$			$v_4$		
	$\pi^\pm$	$K^\pm$	$p + \bar{p}$	$\pi^\pm$	$K^\pm$	$p + \bar{p}$	$\pi^\pm$	$K^\pm$	$p + \bar{p}$
AMPT IC	3-13%	0-16%	0-20%	0-8%	5-12%	0-4%	0-7%	5-12%	0-4%
TRENTTo IC	6-17%	0-19%	3-19%	2-15%	7-22%	0-11%	7-25%	16-28%	0-21%

**Table 6:** The differential  $v_{4,22}$  for different particle species in 10-20% up to 50-60% centrality intervals of Pb–Pb collisions at compared with iEBE-VISHNU hybrid models with two different sets of initial parameters: AMPT initial conditions ( $\eta/s=0.08$  minimum and  $\zeta/s=0$ ) shown in solid bands and TRENTTo initial conditions ( $\eta/s(T)$  and  $\zeta/s(T)$ ) in hatched bands. The bottom panels show maximum value of the difference fit to relative ratios between the measurements data and each model for  $v_n$  ( $n=2,3,4$ ) of  $\pi^\pm$ ,  $K^\pm$  and  $p + \bar{p}$ . The minimum and maximum are obtained from 0-5% up to 40-50% centrality intervals.

Pb–Pb collisions at compared with iEBE-VISHNU hybrid models with two different sets of initial parameters: AMPT initial conditions ( $\eta/s=0.08$  and  $\zeta/s=0$ ) shown in solid bands and TRENTTo initial conditions ( $\eta/s(T)$  and  $\zeta/s(T)$ ) in hatched bands. The bottom panels show the difference between the measurements and each model.

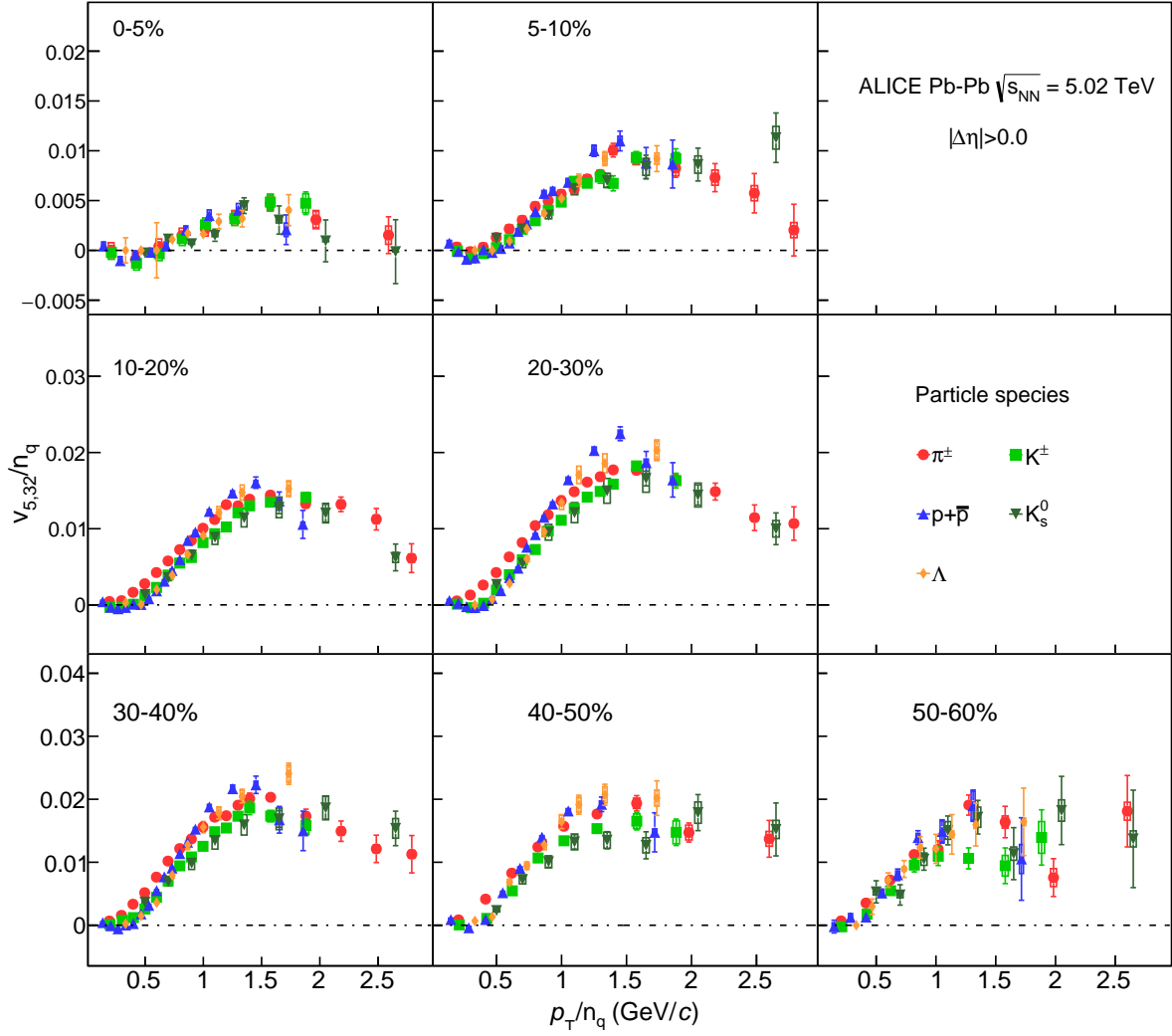


**Figure 11:** The  $p_T/n_q$ -dependence of  $v_{5,32}/n_q$  for different particle species grouped into different centrality intervals of Pb–Pb collisions  $\sqrt{s_{NN}} = 5.02$  TeV

### 6.3 Comparison with $v_n$ of identified particles

The differential  $v_{6,33}$  for different particle species in 10-20% up to 40-50% centrality intervals of Pb–Pb collisions at compared with iEBE-VISHNU hybrid models with two different sets of initial parameters: AMPT initial conditions ( $\eta/s=0.08$  and  $\zeta/s=0$ ) shown in solid bands and TRENTo initial conditions ( $\eta/s(T)$  and  $\zeta/s(T)$ ) in hatched bands. The bottom panels show the difference between the measurements and each model. The features seen in the measurement of non-linear flow modes can be further studied by comparing to that of total flow coefficients. Such comparisons have been performed for  $v_{4,22}(p_T)$  (this study) and  $v_4(p_T)$  measurements [40] by taking the relative difference of pions wrt protons at a given  $p_T$  in both modes. This comparison shows that the observed mass ordering in low  $p_T$  region ( $0 < p_T < 2.5$  GeV/c) is of the same magnitude in  $v_{4,22}$  and  $v_4$ . In the intermediate  $p_T$  region ( $p_T > 2.5$  GeV/c) the observed particle type grouping also shows the same magnitude in both flow modes.

The differential  $v_{6,222}$  for different particle species in 10-20% up to 50-60% centrality intervals of Pb–Pb collisions at compared with iEBE-VISHNU hybrid models with two different sets of initial parameters: AMPT initial conditions ( $\eta/s=0.08$  and  $\zeta/s=0$ ) shown in solid bands and TRENTo initial

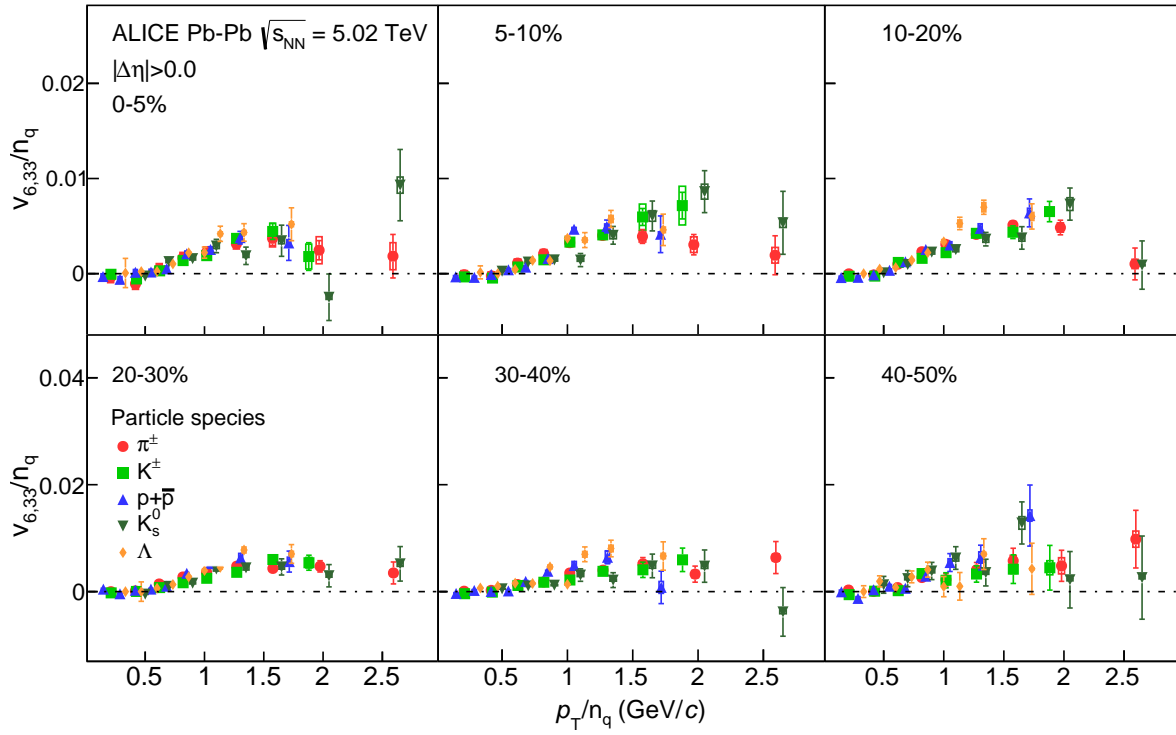


**Figure 12:** The  $p_T/n_q$ -dependence of  $v_{6,33}/n_q$  for different particle species grouped into different centrality intervals of Pb–Pb collisions  $\sqrt{s_{NN}} = 5.02$  TeV

471 conditions ( $\eta/s(T)$  and  $\zeta/s(T)$ ) in hatched bands. The bottom panels show the difference between the  
 472 measurements and each model.

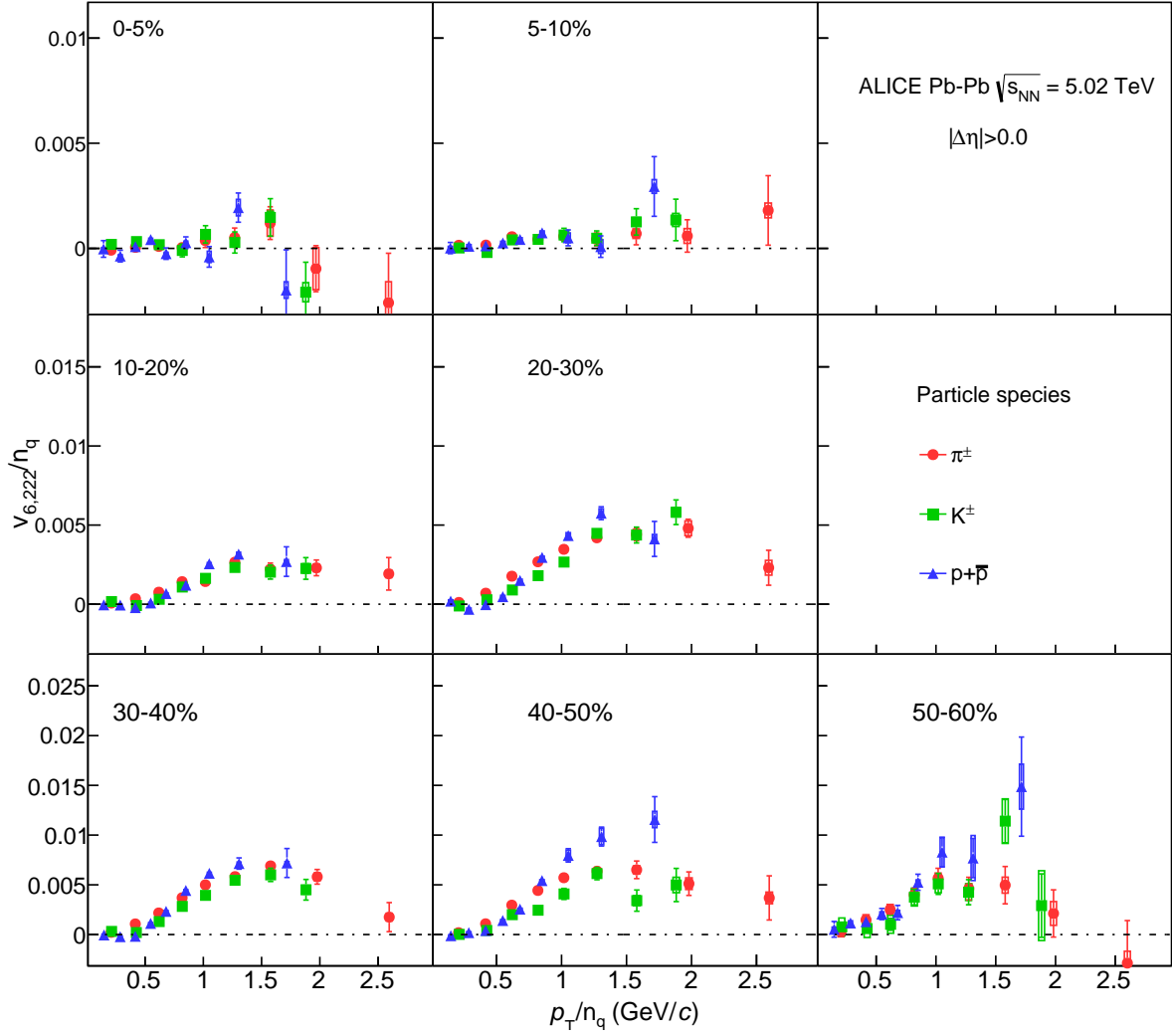


**Figure 13:** The  $p_T/n_q$ -dependence of  $v_{6,222}/n_q$  for different particle species grouped into different centrality intervals of Pb–Pb collisions  $\sqrt{s_{NN}} = 5.02$  TeV

## 7 Summary

In this article, a measurement of non-linear flow modes,  $v_{4,22}$ ,  $v_{5,32}$ ,  $v_{6,222}$  and  $v_{6,33}$  as a function of transverse momentum for different particle species, i.e.  $\pi^\pm$ ,  $K^\pm$ ,  $K_S^0$ ,  $p + \bar{p}$ ,  $\Lambda + \bar{\Lambda}$  and  $\phi$ -meson are reported for a wide range of centrality intervals from 0-5% up to 50-60% in Pb–Pb collisions at  $\sqrt{s_{NN}} = 5.02$  TeV. The non-linear flow modes,  $v_{n,mk}$ , are calculated with a multi-particle correlation technique, namely the generic framework, selecting the identified hadron under study and the reference flow particles from different, non-overlapping pseudorapidity regions.

The magnitude of  $v_{4,22}$ ,  $v_{5,32}$  and  $v_{6,222}$  exhibit a clear centrality dependence. This centrality dependence originates from the contribution of second order flow harmonic, as shown in Eq. 5, and reflects the dependence of  $v_2$  on the anisotropy of the collision geometry. As expected,  $v_{6,33}$  does not exhibit a considerable centrality dependence since  $v_3$  is primarily generated by event-by-event fluctuations of the initial energy density profile. This is supported by the relatively large magnitude of  $v_{6,33}$  in the most-central collisions (0-5%). A clear mass ordering is observed in the low  $p_T$  region ( $p_T < 2.5$  GeV/c). This observation is mass ordering is of the same magnitude as in total flow coefficients and it is associated



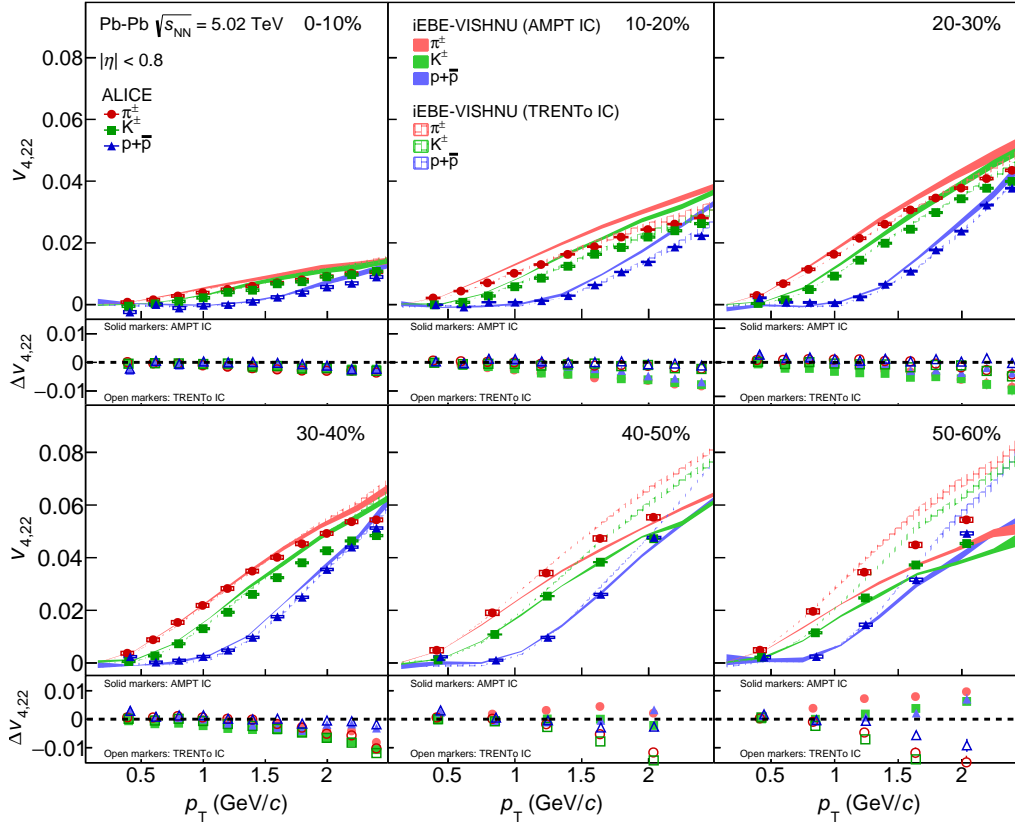


**Figure 14:** The  $p_T$ -differential  $v_{4,22}$  for different particle species in 10-20% up to 50-60% centrality intervals of Pb–Pb collisions at  $\sqrt{s_{NN}} = 5.02$  TeV compared with iEBE-VISHNU hybrid models with two different sets of initial parameters: AMPT initial conditions ( $\eta/s = 0.08$  and  $\zeta/s = 0$ ) shown in solid bands and TRENTo initial conditions ( $\eta/s(T)$  and  $\zeta/s(T)$ ) in hatched bands. The bottom panels show the difference between the measurements and each model.

with the interplay between the anisotropic flow and radial flow. In the intermediate  $p_T$  region ( $p_T > 2.5$  GeV/c), a particle type grouping is observed where the magnitude of non-linear modes for baryons are larger than for mesons. [This particle type grouping is similar to that observed in total flow coefficients.](#) The NCQ scaling holds at **best in** an approximate level of  $\pm 20\%$  within the current level of statistical and systematic uncertainties similar to that of total flow coefficients [40].

The comparison of two models based on the iEBE-VISHNU hybrid model, and with two different initial conditions (AMPT and TRENTo) and transport properties show that neither of the models are able to fully describe the measurements. This varies depending on the centrality percentile and particle species similar to the model-data comparison for anisotropic flow [40]. Measurements are better predicted by the models in more central collisions. All in all, the model using AMPT initial conditions ( $\eta/s = 0.08$  and  $\zeta/s = 0$ ) exhibits a magnitude and shape closer to the measurements. As a result, in order to further constrain the values of transport properties and the initial conditions of the system, it is necessary to tune the input parameters of future hydrodynamic calculations attempting to describe these measurements.

## Acknowledgements

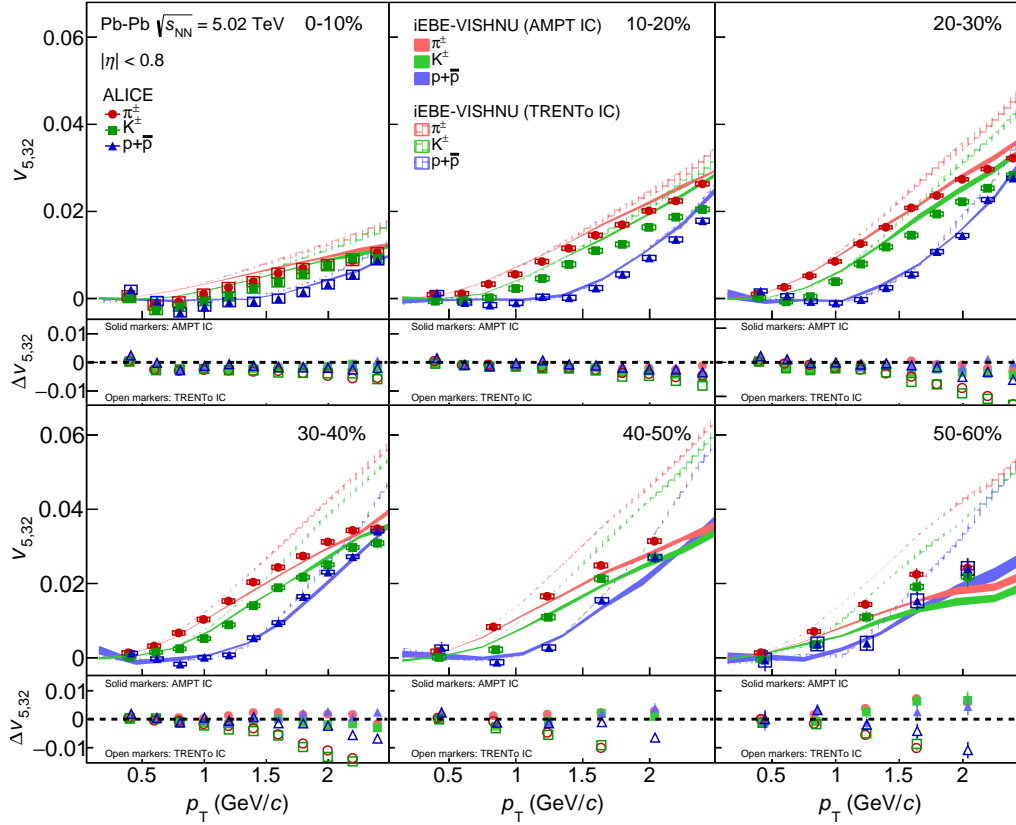


**Figure 15:** The  $p_T$ -differential  $v_{5,32}$  for different particle species in 10-20% up to 50-60% centrality intervals of Pb–Pb collisions at  $\sqrt{s_{NN}} = 5.02$  TeV compared with iEBE-VISHNU hybrid models with two different sets of initial parameters: AMPT initial conditions ( $\eta/s = 0.08$  and  $\zeta/s = 0$ ) shown in solid bands and TRENTo initial conditions ( $\eta/s(T)$  and  $\zeta/s(T)$ ) in hatched bands. The bottom panels show the difference between the measurements and each model.

## References

- [1] S. Borsanyi, G. Endrodi, Z. Fodor, A. Jakovac, S. D. Katz, S. Krieg, C. Ratti, and K. K. Szabo, “The QCD equation of state with dynamical quarks”, *JHEP* **11** (2010), arXiv:1007.2580 [hep-lat].
- [2] T. Bhattacharya *et al.*, “QCD Phase Transition with Chiral Quarks and Physical Quark Masses”, *Phys. Rev. Lett.* **113** no. 8, (2014), arXiv:1402.5175 [hep-lat].
- [3] E. V. Shuryak, “Theory and phenomenology of the QCD vacuum”, *Phys. Rept.* **115** (1984).
- [4] J. Cleymans, R. V. Gavai, and E. Suhonen, “Quarks and Gluons at High Temperatures and Densities”, *Phys. Rept.* **130** (1986).
- [5] S. A. Bass, M. Gyulassy, H. Stoecker, and W. Greiner, “Signatures of quark gluon plasma formation in high-energy heavy ion collisions: A Critical review”, *J. Phys.* **G25** (1999), arXiv:hep-ph/9810281 [hep-ph].
- [6] R. S. Bhalerao and J.-Y. Ollitrault, “Eccentricity fluctuations and elliptic flow at RHIC”, *Phys. Lett.* **B641** (2006), arXiv:nucl-th/0607009 [nucl-th].

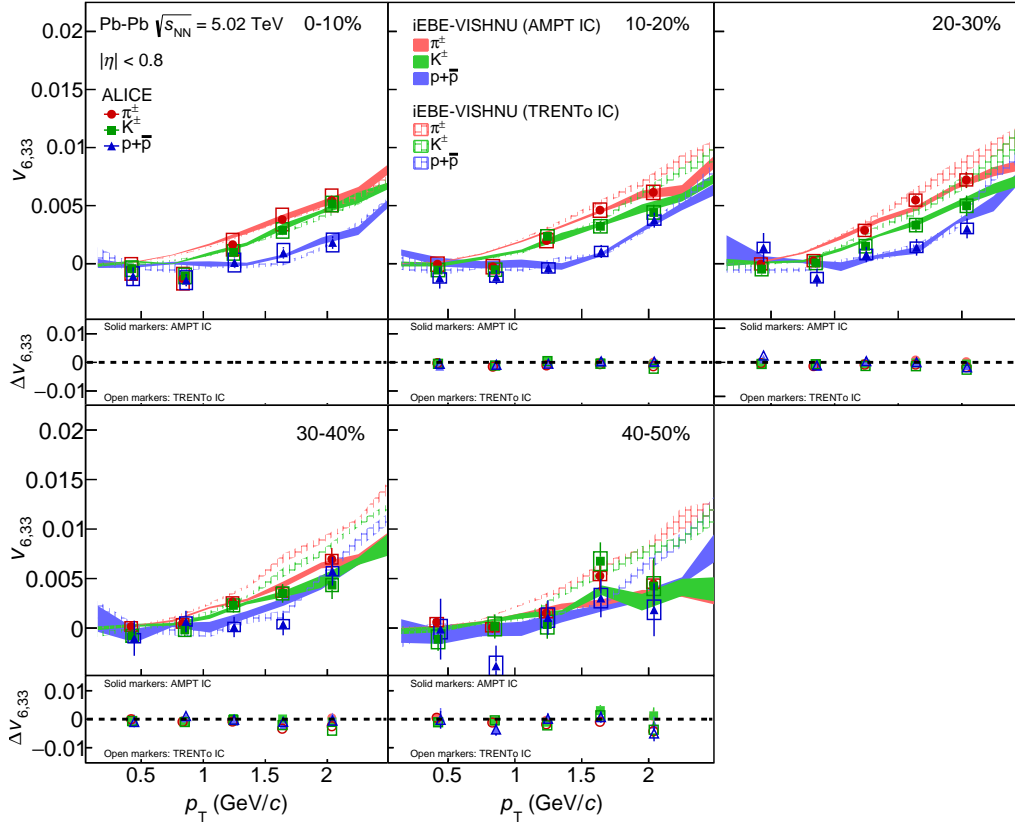


**Figure 16:** The  $p_T$ -differential  $v_{6,33}$  for different particle species in 10-20% up to 40-50% centrality intervals of Pb–Pb collisions at  $\sqrt{s_{NN}} = 5.02$  TeV compared with iEBE-VISHNU hybrid models with two different sets of initial parameters: AMPT initial conditions ( $\eta/s = 0.08$  and  $\zeta/s = 0$ ) shown in solid bands and TRENTo initial conditions ( $\eta/s(T)$  and  $\zeta/s(T)$ ) in hatched bands. The bottom panels show the difference between the measurements and each model.

- [7] B. Alver *et al.*, “Importance of correlations and fluctuations on the initial source eccentricity in high-energy nucleus-nucleus collisions”, *Phys. Rev.* **C77** (2008), arXiv:0711.3724 [nucl-ex].
- [8] B. Alver and G. Roland, “Collision geometry fluctuations and triangular flow in heavy-ion collisions”, *Phys. Rev.* **C81** (2010), arXiv:1003.0194 [nucl-th]. [Erratum: *Phys. Rev.* **C82**, 039903(2010)].
- [9] B. H. Alver, C. Gombeaud, M. Luzum, and J.-Y. Ollitrault, “Triangular flow in hydrodynamics and transport theory”, *Phys. Rev.* **C82** (2010), arXiv:1007.5469 [nucl-th].
- [10] **PHOBOS** Collaboration, S. Manly *et al.*, “System size, energy and pseudorapidity dependence of directed and elliptic flow at RHIC”, *Nucl. Phys.* **A774** (2006), arXiv:nucl-ex/0510031 [nucl-ex].
- [11] S. Voloshin and Y. Zhang, “Flow study in relativistic nuclear collisions by Fourier expansion of Azimuthal particle distributions”, *Z. Phys.* **C70** (1996), arXiv:hep-ph/9407282 [hep-ph].  
~~A. M. Poskanzer and~~
- [12] S. A. Voloshin, “~~Methods for analyzing anisotropic flow in relativistic nuclear collisions~~ Toward the energy and the system size dependence of elliptic flow: Working on flow fluctuations”, ~~, in 22nd~~

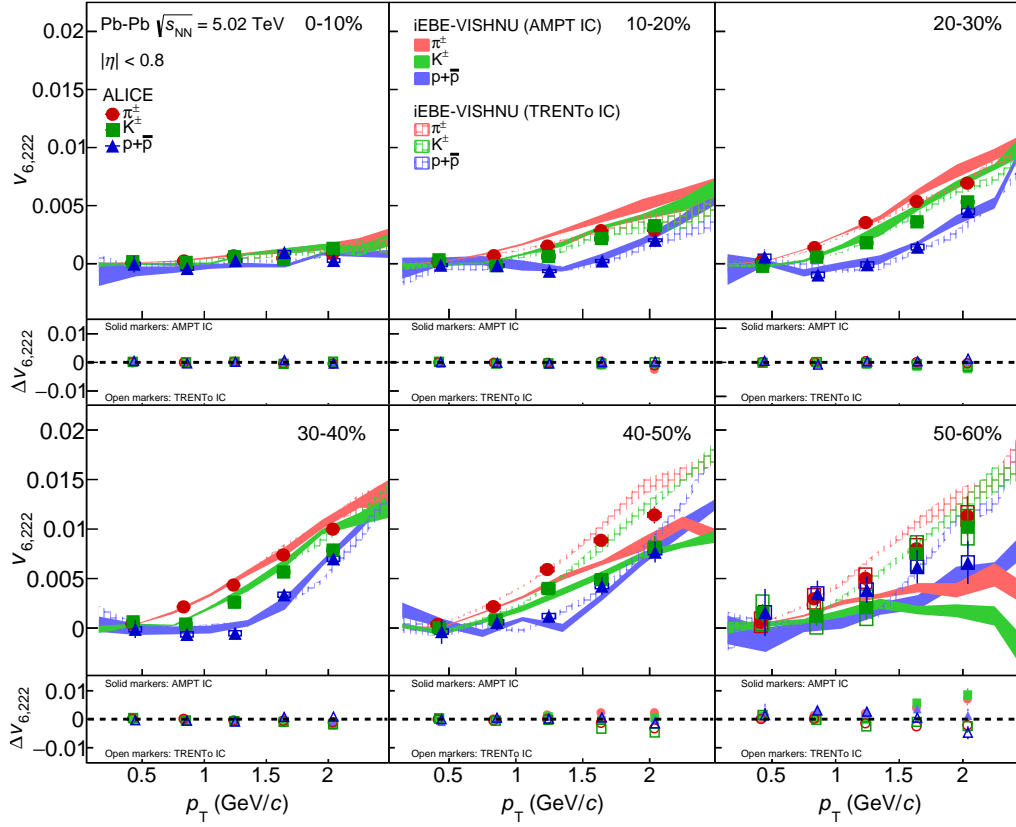


**Figure 17:** The  $p_T$ -differential  $v_{6,222}$  for different particle species in 10-20% up to 50-60% centrality intervals of Pb–Pb collisions at  $\sqrt{s_{NN}} = 5.02$  TeV compared with iEBE-VISHNU hybrid models with two different sets of initial parameters: AMPT initial conditions ( $\eta/s = 0.08$  and  $\zeta/s = 0$ ) shown in solid bands and TRENTo initial conditions ( $\eta/s(T)$  and  $\zeta/s(T)$ ) in hatched bands. The bottom panels show the difference between the measurements and each model.

[Winter Workshop on Nuclear Dynamics \(WWND 2006\) La Jolla, California, March 11-19, 2006.](#)  
[2006. arXiv:nuc1-th/0606022 \[nuc1-th\].](#)

- [13] **STAR** Collaboration, J. Adams *et al.*, “Particle type dependence of azimuthal anisotropy and nuclear modification of particle production in Au + Au collisions at  $\sqrt{s_{NN}} = 200$  GeV”, *Phys. Rev. Lett.* **92** (2004), arXiv:nuc1-ex/0306007 [nuc1-ex].
- [14] **STAR** Collaboration, B. I. Abelev *et al.*, “Mass, quark-number, and  $\sqrt{s_{NN}}$  dependence of the second and fourth flow harmonics in ultra-relativistic nucleus-nucleus collisions”, *Phys. Rev.* **C75** (2007), arXiv:nuc1-ex/0701010 [nuc1-ex].
- [15] **PHENIX** Collaboration, S. S. Adler *et al.*, “Elliptic flow of identified hadrons in Au+Au collisions at  $\sqrt{s_{NN}} = 200$  GeV”, *Phys. Rev. Lett.* **91** (2003), arXiv:nuc1-ex/0305013 [nuc1-ex].
- [16] **PHENIX** Collaboration, A. Adare *et al.*, “Scaling properties of azimuthal anisotropy in Au+Au and Cu+Cu collisions at  $s(NN) = 200$ -GeV”, *Phys. Rev. Lett.* **98** (2007), arXiv:nuc1-ex/0608033 [nuc1-ex].
- [17] **PHOBOS** Collaboration, B. Alver *et al.*, “Event-by-Event Fluctuations of Azimuthal Particle Anisotropy in Au + Au Collisions at  $\sqrt{s_{NN}} = 200$  GeV”, *Phys. Rev. Lett.* **104** (2010), arXiv:nuc1-ex/0702036 [nuc1-ex].

- [18] [PHENIX Collaboration, K. Adcox \*et al.\*, “Flow measurements via two particle azimuthal correlations in Au+Au collisions at  \$\sqrt{s\_{NN}} = 130\$ -GeV”, \*Phys. Rev. Lett.\* \*\*89\*\* \(2002\), arXiv:nuc1-ex/0204005 \[nucl-ex\]](#).
- [19] [STAR Collaboration, L. Adamczyk \*et al.\*, “Elliptic flow of identified hadrons in Au+Au collisions at  \$\sqrt{s\_{NN}} = 7.7\$ -62.4 GeV”, \*Phys. Rev.\* \*\*C88\*\* \(2013\), arXiv:1301.2348 \[nucl-ex\]](#).
- [20] [PHENIX Collaboration, S. S. Adler \*et al.\*, “Saturation of azimuthal anisotropy in Au + Au collisions at  \$\sqrt{s\_{NN}} = 62\$ -GeV to 200-GeV”, \*Phys. Rev. Lett.\* \*\*94\*\* \(2005\), arXiv:nuc1-ex/0411040 \[nucl-ex\]](#).
- [21] [PHENIX Collaboration, S. Afanasiev \*et al.\*, “Systematic Studies of Elliptic Flow Measurements in Au+Au Collisions at  \$\sqrt{s\_{NN}} = 200\$ -GeV”, \*Phys. Rev.\* \*\*C80\*\* \(2009\), arXiv:0905.1070 \[nucl-ex\]](#).
- [22] [PHENIX Collaboration, A. Adare \*et al.\*, “Measurements of Higher-Order Flow Harmonics in Au+Au Collisions at  \$\sqrt{s\_{NN}} = 200\$  GeV”, \*Phys. Rev. Lett.\* \*\*107\*\* \(2011\), arXiv:1105.3928 \[nucl-ex\]](#).
- [23] [STAR Collaboration, K. H. Ackermann \*et al.\*, “Elliptic flow in Au + Au collisions at  \$\sqrt{s\_{NN}} = 130\$  GeV”, \*Phys. Rev. Lett.\* \*\*86\*\* \(2001\), arXiv:nuc1-ex/0009011 \[nucl-ex\]](#).
- [24] [STAR Collaboration, C. Adler \*et al.\*, “Identified particle elliptic flow in Au + Au collisions at  \$\sqrt{s\_{NN}} = 130\$ -GeV”, \*Phys. Rev. Lett.\* \*\*87\*\* \(2001\), arXiv:nuc1-ex/0107003 \[nucl-ex\]](#).
- [25] [STAR Collaboration, C. Adler \*et al.\*, “Azimuthal anisotropy and correlations in the hard scattering regime at RHIC”, \*Phys. Rev. Lett.\* \*\*90\*\* \(2003\), arXiv:nuc1-ex/0206006 \[nucl-ex\]](#).
- [26] [STAR Collaboration, C. Adler \*et al.\*, “Elliptic flow from two and four particle correlations in Au+Au collisions at  \$\sqrt{s\_{NN}} = 130\$  GeV”, \*Phys. Rev.\* \*\*C66\*\* \(2002\), arXiv:nuc1-ex/0206001 \[nucl-ex\]](#).
- [27] [STAR Collaboration, J. Adams \*et al.\*, “Azimuthal anisotropy at RHIC: The First and fourth harmonics”, \*Phys. Rev. Lett.\* \*\*92\*\* \(2004\), arXiv:nuc1-ex/0310029 \[nucl-ex\]](#).
- [28] [STAR Collaboration, J. Adams \*et al.\*, “Azimuthal anisotropy and correlations at large transverse momenta in p+p and Au+Au collisions at  \$\sqrt{s\_{NN}} = 200\$  GeV”, \*Phys. Rev. Lett.\* \*\*93\*\* \(2004\), arXiv:nuc1-ex/0407007 \[nucl-ex\]](#).
- [29] [STAR Collaboration, J. Adams \*et al.\*, “Azimuthal anisotropy in Au+Au collisions at  \$\sqrt{s\_{NN}} = 200\$ -GeV”, \*Phys. Rev.\* \*\*C72\*\* \(2005\), arXiv:nuc1-ex/0409033 \[nucl-ex\]](#).
- [30] [ALICE Collaboration, K. Aamodt \*et al.\*, “Elliptic flow of charged particles in Pb-Pb collisions at 2.76 TeV”, \*Phys. Rev. Lett.\* \*\*105\*\* \(2010\), arXiv:1011.3914 \[nucl-ex\]](#).
- [31] [ALICE Collaboration, K. Aamodt \*et al.\*, “Higher harmonic anisotropic flow measurements of charged particles in Pb-Pb collisions at  \$\sqrt{s\_{NN}} = 2.76\$  TeV”, \*Phys. Rev. Lett.\* \*\*107\*\* \(2011\), arXiv:1105.3865 \[nucl-ex\]](#).
- [32] [ALICE Collaboration, B. Abelev \*et al.\*, “Anisotropic flow of charged hadrons, pions and \(anti-\)protons measured at high transverse momentum in Pb-Pb collisions at  \$\sqrt{s\_{NN}} = 2.76\$  TeV”, \*Phys. Lett.\* \*\*B719\*\* \(2013\), arXiv:1205.5761 \[nucl-ex\]](#).
- [33] [CMS Collaboration, S. Chatrchyan \*et al.\*, “Azimuthal anisotropy of charged particles at high transverse momenta in PbPb collisions at  \$\sqrt{s\_{NN}} = 2.76\$  TeV”, \*Phys. Rev. Lett.\* \*\*109\*\* \(2012\), arXiv:1204.1850 \[nucl-ex\]](#).

- [34] [CMS Collaboration, S. Chatrchyan \*et al.\*, “Measurement of the elliptic anisotropy of charged particles produced in PbPb collisions at  \$\sqrt{s\_{NN}}=2.76\$  TeV”, \*Phys. Rev.\* \*\*C87\*\* no. 1, \(2013\), arXiv:1204.1409 \[nucl-ex\]](#).
- [35] [ATLAS Collaboration, G. Aad \*et al.\*, “Measurement of the pseudorapidity and transverse momentum dependence of the elliptic flow of charged particles in lead-lead collisions at  \$\sqrt{s\_{NN}} = 2.76\$  TeV with the ATLAS detector”, \*Phys. Lett.\* \*\*B707\*\* \(2012\), arXiv:1108.6018 \[hep-ex\]](#).
- [36] [ATLAS Collaboration, G. Aad \*et al.\*, “Measurement of the azimuthal anisotropy for charged particle production in  \$\sqrt{s\_{NN}} = 2.76\$  TeV lead-lead collisions with the ATLAS detector”, \*Phys. Rev.\* \*\*C86\*\* \(2012\), arXiv:1203.3087 \[hep-ex\]](#).
- [37] ALICE Collaboration, B. B. Abelev *et al.*, “Elliptic flow of identified hadrons in Pb-Pb collisions at  $\sqrt{s_{NN}} = 2.76$  TeV”, *JHEP* **06** (2015), arXiv:1405.4632 [nucl-ex].
- [38] ALICE Collaboration, J. Adam *et al.*, “Higher harmonic flow coefficients of identified hadrons in Pb-Pb collisions at  $\sqrt{s_{NN}} = 2.76$  TeV”, *JHEP* **09** (2016), arXiv:1606.06057 [nucl-ex].
- [39] [ALICE Collaboration, J. Adam \*et al.\*, “Anisotropic flow of charged particles in Pb-Pb collisions at  \$\sqrt{s\_{NN}} = 5.02\$  TeV”, \*Phys. Rev. Lett.\* \*\*116\*\* no. 13, \(2016\), arXiv:1602.01119 \[nucl-ex\]](#).
- [40] ALICE Collaboration, S. Acharya *et al.*, “Anisotropic flow of identified particles in Pb-Pb collisions at  $\sqrt{s_{NN}} = 5.02$  TeV”, *JHEP* **09** (2018), arXiv:1805.04390 [nucl-ex].
- [41] P. Kovtun, D. T. Son, and A. O. Starinets, “Viscosity in strongly interacting quantum field theories from black hole physics”, *Phys. Rev. Lett.* **94** (2005), arXiv:hep-th/0405231 [hep-th].
- ~~ALICE Collaboration, J. Adam *et al.*~~
- [42] [H. Niemi, K. J. Eskola, R. Paatelainen, and K. Tuominen, “Anisotropic flow of charged particles in Pb-Pb collisions at  \$\sqrt{s\_{NN}} = 5.02\$  TeV Predictions for 5.023 TeV Pb + Pb collisions at the CERN Large Hadron Collider”, \*Phys. Rev.\* \*\*C93\*\* no. 1, \(2016\), arXiv:1511.04296 \[hep-ph\]](#).
- [43] D. Teaney and L. Yan, “Triangularity and Dipole Asymmetry in Heavy Ion Collisions”, *Phys. Rev.* **C83** (2011), arXiv:1010.1876 [nucl-th].
- [44] D. Teaney and L. Yan, “Event-plane correlations and hydrodynamic simulations of heavy ion collisions”, *Phys. Rev.* **C90** no. 2, (2014), arXiv:1312.3689 [nucl-th].
- ~~R. S. Bhalerao, J.-Y. Ollitrault, and S. Pal, “Characterizing flow fluctuations with moments”,~~
- [45] J. Qian, U. Heinz, R. He, and L. Huo, “Differential flow correlations in relativistic heavy-ion collisions”, *Phys. Rev.* **C95** no. 5, (2017), arXiv:1703.04077 [nucl-th].
- [46] [R. S. Bhalerao, J.-Y. Ollitrault, and S. Pal, “Characterizing flow fluctuations with moments”, \*Phys. Lett.\* \*\*B742\*\* \(2015\), arXiv:1411.5160 \[nucl-th\]](#).
- [47] L. Yan and J.-Y. Ollitrault, “ $v_4, v_5, v_6, v_7$ : nonlinear hydrodynamic response versus LHC data”, *Phys. Lett.* **B744** (2015), arXiv:1502.02502 [nucl-th].
- [48] ALICE Collaboration, S. Acharya *et al.*, “Linear and non-linear flow modes in Pb-Pb collisions at  $\sqrt{s_{NN}} = 2.76$  TeV”, *Phys. Lett.* **B773** (2017), arXiv:1705.04377 [nucl-ex].
- ~~ALICE Collaboration, K. Aamodt *et al.*, “Higher harmonic anisotropic flow measurements of charged particles in Pb-Pb collisions at  $\sqrt{s_{NN}}=2.76$  TeV”,~~
- ~~ATLAS Collaboration, G. Aad *et al.*, “Measurement of the azimuthal anisotropy for charged particle production in  $\sqrt{s_{NN}} = 2.76$  TeV lead-lead collisions with the ATLAS detector”,~~



- [49] **CMS** Collaboration, S. Chatrchyan *et al.*, “Measurement of higher-order harmonic azimuthal anisotropy in PbPb collisions at  $\sqrt{s_{NN}} = 2.76$  TeV”, *Phys. Rev.* **C89** no. 4, (2014), arXiv:1310.8651 [nucl-ex].
- [50] **ALICE** Collaboration, S. Acharya *et al.*, “Energy dependence and fluctuations of anisotropic flow in Pb-Pb collisions at  $\sqrt{s_{NN}} = 5.02$  and 2.76 TeV”, *JHEP* **07** (2018), arXiv:1804.02944 [nucl-ex].
- [51] S. A. Voloshin, “Transverse radial expansion and directed flow”, *Phys. Rev.* **C55** (1997), arXiv:nucl-th/9611038 [nucl-th].
- [52] P. Huovinen, P. F. Kolb, U. W. Heinz, P. V. Ruuskanen, and S. A. Voloshin, “Radial and elliptic flow at RHIC: Further predictions”, *Phys. Lett.* **B503** (2001), arXiv:hep-ph/0101136 [hep-ph].
- [53] **ALICE** Collaboration, J. Adam *et al.*, “Event shape engineering for inclusive spectra and elliptic flow in Pb-Pb collisions at  $\sqrt{s_{NN}} = 2.76$  TeV”, *Phys. Rev.* **C93** no. 3, (2016), arXiv:1507.06194 [nucl-ex].
- [54] S. A. Voloshin, “Anisotropic flow”, *Nucl. Phys.* **A715** (2003), arXiv:nucl-ex/0210014 [nucl-ex].
- [55] D. Molnar and S. A. Voloshin, “Elliptic flow at large transverse momenta from quark coalescence”, *Phys. Rev. Lett.* **91** (2003), arXiv:nucl-th/0302014 [nucl-th].
- [56] **PHENIX** Collaboration, A. Adare *et al.*, “Deviation from quark-number scaling of the anisotropy parameter  $v_2$  of pions, kaons, and protons in Au+Au collisions at  $\sqrt{s_{NN}} = 200$  GeV”, *Phys. Rev.* **C85** (2012), arXiv:1203.2644 [nucl-ex].
- [57] [X. Zhu, Y. Zhou, H. Xu, and H. Song](#), “Correlations of flow harmonics in 2.76A TeV Pb–Pb collisions”, *Phys. Rev.* **C95** no. 4, (2017), arXiv:1608.05305 [nucl-th].
- [58] **ALICE** Collaboration, K. Aamodt *et al.*, “The ALICE experiment at the CERN LHC”, *JINST* **3** (2008).
- [59] **ALICE** Collaboration, B. B. Abelev *et al.*, “Performance of the ALICE Experiment at the CERN LHC”, *Int. J. Mod. Phys.* **A29** (2014), arXiv:1402.4476 [nucl-ex].
- [60] **ALICE** Collaboration, K. Aamodt *et al.*, “Charged-particle multiplicity density at mid-rapidity in central Pb-Pb collisions at  $\sqrt{s_{NN}} = 2.76$  TeV”, *Phys. Rev. Lett.* **105** (2010), arXiv:1011.3916 [nucl-ex].
- [61] J. Alme *et al.*, “The ALICE TPC, a large 3-dimensional tracking device with fast readout for ultra-high multiplicity events”, *Nucl. Instrum. Meth.* **A622** (2010), arXiv:1001.1950 [physics.ins-det].
- [62] **ALICE** Collaboration, E. Abbas *et al.*, “Performance of the ALICE VZERO system”, *JINST* **8** (2013), arXiv:1306.3130 [nucl-ex].
- [63] **ALICE** Collaboration, B. Abelev *et al.*, “Centrality determination of Pb-Pb collisions at  $\sqrt{s_{NN}} = 2.76$  TeV with ALICE”, *Phys. Rev.* **C88** no. 4, (2013), arXiv:1301.4361 [nucl-ex].
- [64] P. Billoir, “Track Fitting With Multiple Scattering: A New Method”, *Nucl. Instrum. Meth.* **A225** (1984).

- [65] P. Billoir, R. Fruhwirth, and M. Regler, “TRACK ELEMENT MERGING STRATEGY AND VERTEX FITTING IN COMPLEX MODULAR DETECTORS”, *Nucl. Instrum. Meth.* **A241** (1985) .
- [66] ALICE Collaboration, B. Abelev *et al.*, “Centrality dependence of  $\pi$ , K, p production in Pb-Pb collisions at  $\sqrt{s_{NN}} = 2.76$  TeV”, *Phys. Rev.* **C88** (2013) , arXiv:1303.0737 [hep-ex].
- [67] K. Olive, “Review of particle physics”, *Chinese Physics C* **40** no. 10, (Oct, 2016) .
- [68] J. Podolanski and R. Armenteros, “Iii. analysis of v-events”, *The London, Edinburgh, and Dublin Philosophical Magazine and Journal of Science* **45** no. 360, (1954) .
- [69] ALICE Collaboration, J. Adam *et al.*, “Particle identification in ALICE: a Bayesian approach”, arXiv:1602.01392 [physics.data-an].
- [70] A. Bilandzic, C. H. Christensen, K. Gulbrandsen, A. Hansen, and Y. Zhou, “Generic framework for anisotropic flow analyses with multiparticle azimuthal correlations”, *Phys. Rev.* **C89** no. 6, (2014) , arXiv:1312.3572 [nucl-ex].
- [71] R. Barlow, “Systematic errors: Facts and fictions”, in *Advanced Statistical Techniques in Particle Physics. Proceedings, Conference, Durham, UK, March 18-22, 2002*, pp. 134–144. 2002. arXiv:hep-ex/0207026 [hep-ex].  
<http://www.ipp.dur.ac.uk/Workshops/02/statistics/proceedings//barlow.pdf>.
- [72] C. Shen, U. Heinz, P. Huovinen, and H. Song, “Radial and elliptic flow in Pb+Pb collisions at the Large Hadron Collider from viscous hydrodynamic”, *Phys. Rev.* **C84** (2011) , arXiv:1105.3226 [nucl-th].
- [73] H.-J. Xu, Z. Li, and H. Song, “High order flow harmonics of identified hadrons in 2.76 A TeV Pb+Pb collisions”, arXiv:1602.02029 [nucl-th].
- [74] S. McDonald, C. Shen, F. Fillion-Gourdeau, S. Jeon, and C. Gale, “Hydrodynamic predictions for Pb+Pb collisions at 5.02 TeV”, *Phys. Rev.* **C95** no. 6, (2017) , arXiv:1609.02958 [hep-ph].
- [75] W. Zhao, H.-j. Xu, and H. Song, “Collective flow in 2.76 A TeV and 5.02 A TeV Pb+Pb collisions”, *Eur. Phys. J.* **C77** no. 9, (2017) , arXiv:1703.10792 [nucl-th].
- [76] C. Shen, Z. Qiu, H. Song, J. Bernhard, S. Bass, and U. Heinz, “The iEBE-VISHNU code package for relativistic heavy-ion collisions”, *Comput. Phys. Commun.* **199** (2016) , arXiv:1409.8164 [nucl-th].
- [77] H. Song, S. A. Bass, and U. Heinz, “Viscous QCD matter in a hybrid hydrodynamic+Boltzmann approach”, *Phys. Rev.* **C83** (2011) , arXiv:1012.0555 [nucl-th].
- [78] H. Song and U. W. Heinz, “Suppression of elliptic flow in a minimally viscous quark-gluon plasma”, *Phys. Lett.* **B658** (2008) , arXiv:0709.0742 [nucl-th].
- [79] Z.-W. Lin, C. M. Ko, B.-A. Li, B. Zhang, and S. Pal, “A Multi-phase transport model for relativistic heavy ion collisions”, *Phys. Rev.* **C72** (2005) , arXiv:nucl-th/0411110 [nucl-th].
- [80] J. S. Moreland, J. E. Bernhard, and S. A. Bass, “Alternative ansatz to wounded nucleon and binary collision scaling in high-energy nuclear collisions”, *Phys. Rev.* **C92** no. 1, (2015) , arXiv:1412.4708 [nucl-th].
- [81] J. E. Bernhard, J. S. Moreland, S. A. Bass, J. Liu, and U. Heinz, “Applying Bayesian parameter estimation to relativistic heavy-ion collisions: simultaneous characterization of the initial state and quark-gluon plasma medium”, *Phys. Rev.* **C94** no. 2, (2016) , arXiv:1605.03954 [nucl-th].



## A Additional figures

### A.1 $KE_T$ scaling

One suggestion to further study the scaling properties of flow coefficients was to extend the scaling to lower  $p_T$  values by studying the transverse kinetic energy dependence of anisotropic flow harmonics. Transverse kinetic energy is defined as  $KE_T = m_T - m_0$ , where  $m_T = \sqrt{m_0^2 + p_T^2}$  is the transverse mass. Figures A.1, A.2, A.3 and A.4 present  $KE_T$  scaling for  $v_{4,22}$ ,  $v_{5,32}$ ,  $v_{6,33}$  and  $v_{6,222}$  respectively, for  $\pi^\pm$ ,  $K^\pm$ ,  $p + \bar{p}$ ,  $K_S^0$ ,  $\Lambda + \bar{\Lambda}$  and  $\phi$ -meson grouped in different centrality intervals.

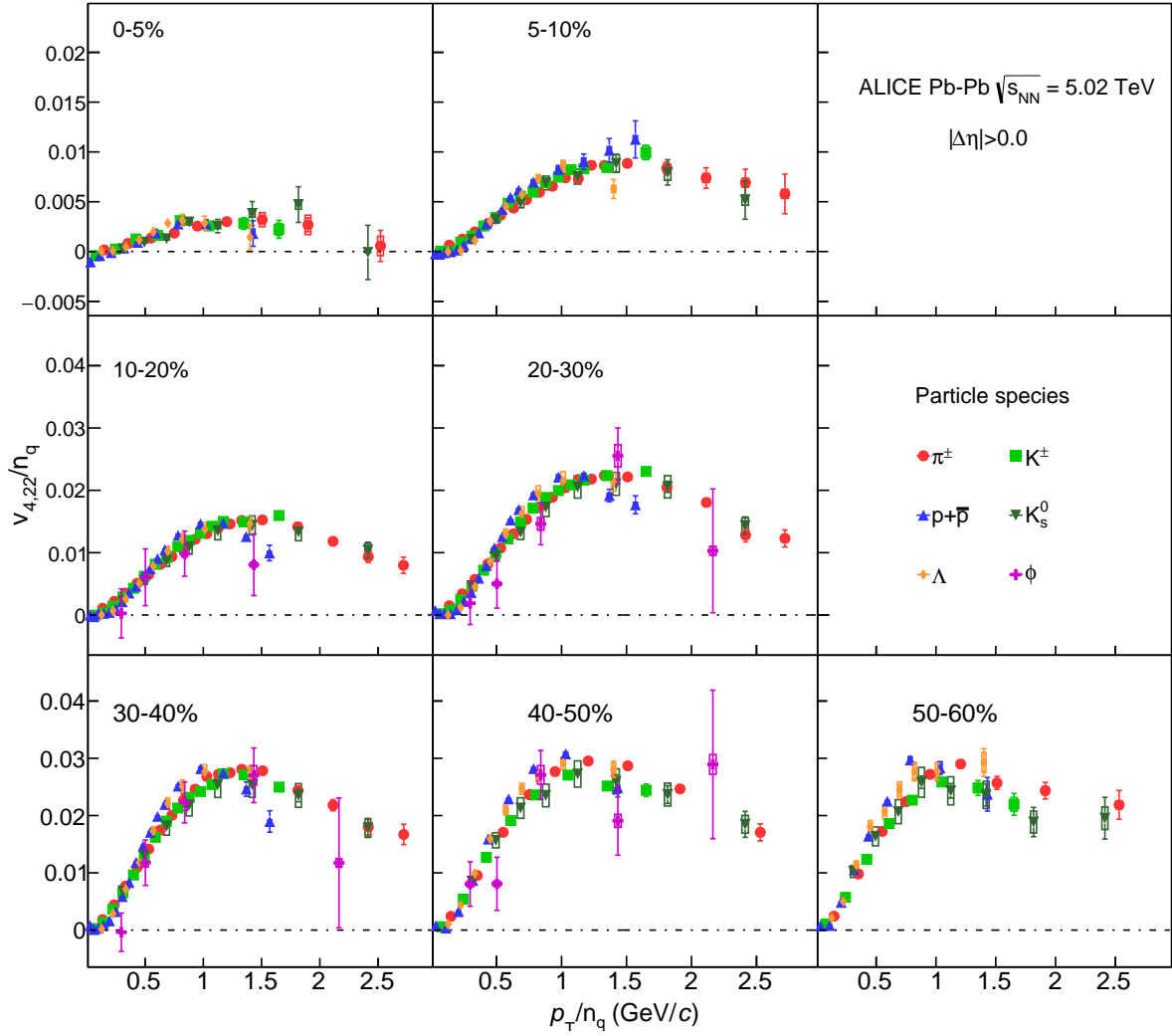


**Figure A.1:** The  $(m_T - m_0)/n_q$ -dependence of  $v_{4,22}/n_q$  for different particle species grouped into different centrality intervals of Pb–Pb collisions  $\sqrt{s_{NN}} = 5.02$  TeV

## B The ALICE Collaboration

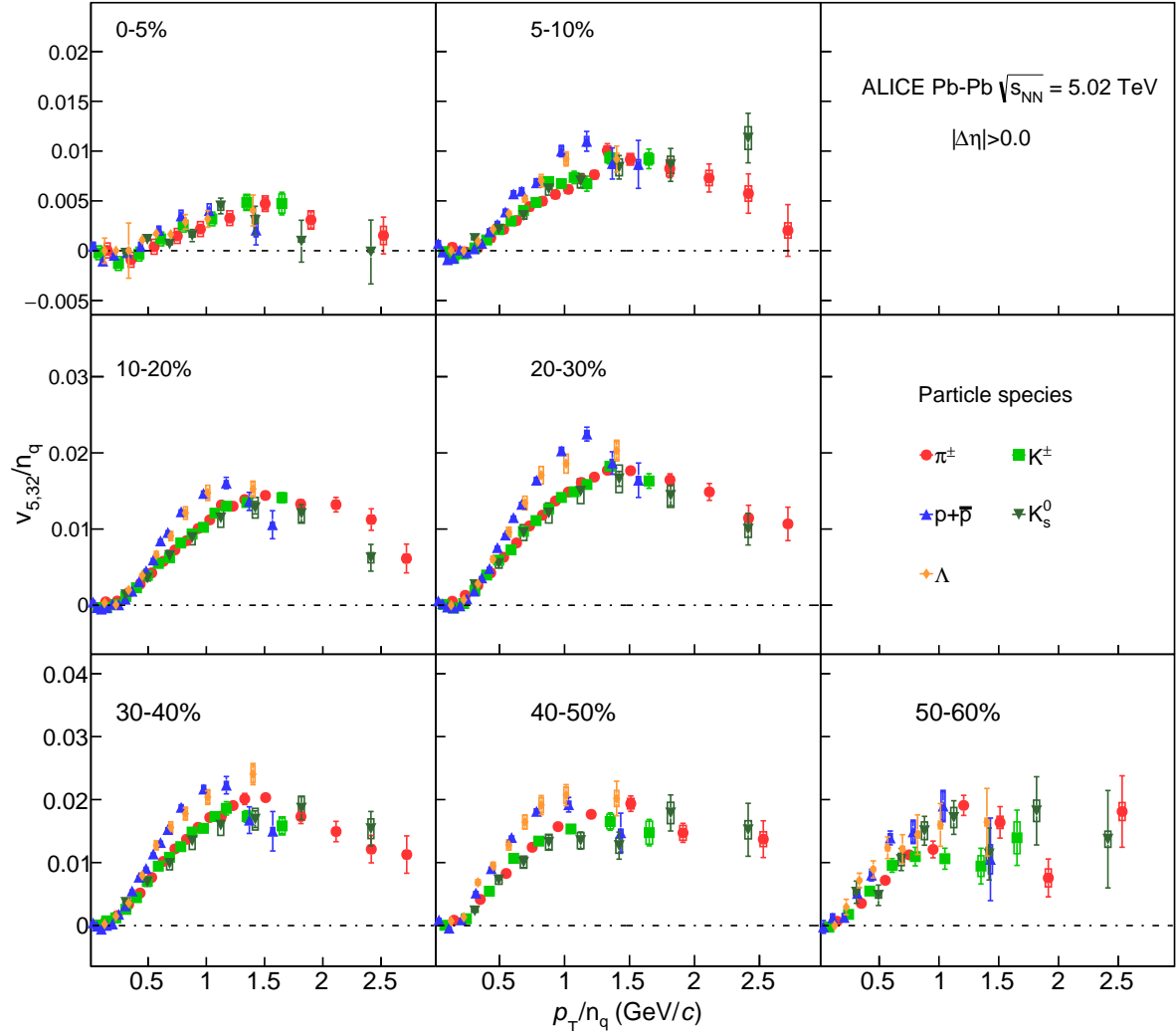


**Figure A.2:** The  $(m_T - m_0)/n_q$ -dependence of  $v_{5,32}/n_q$  for different particle species grouped into different centrality intervals of Pb–Pb collisions  $\sqrt{s_{NN}} = 5.02$  TeV

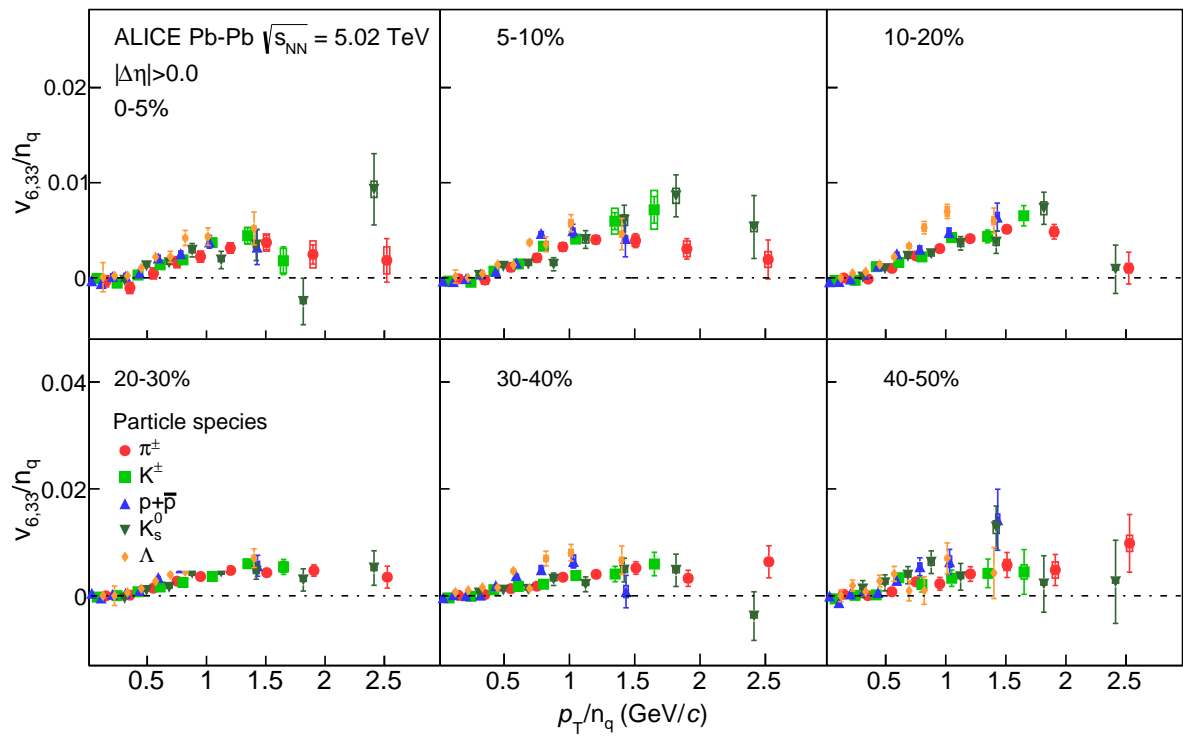


**Figure A.3:** The  $(m_T - m_0)/n_q$ -dependence of  $v_{6,33}/n_q$  for different particle species grouped into different centrality intervals of Pb–Pb collisions  $\sqrt{s_{\text{NN}}} = 5.02$  TeV

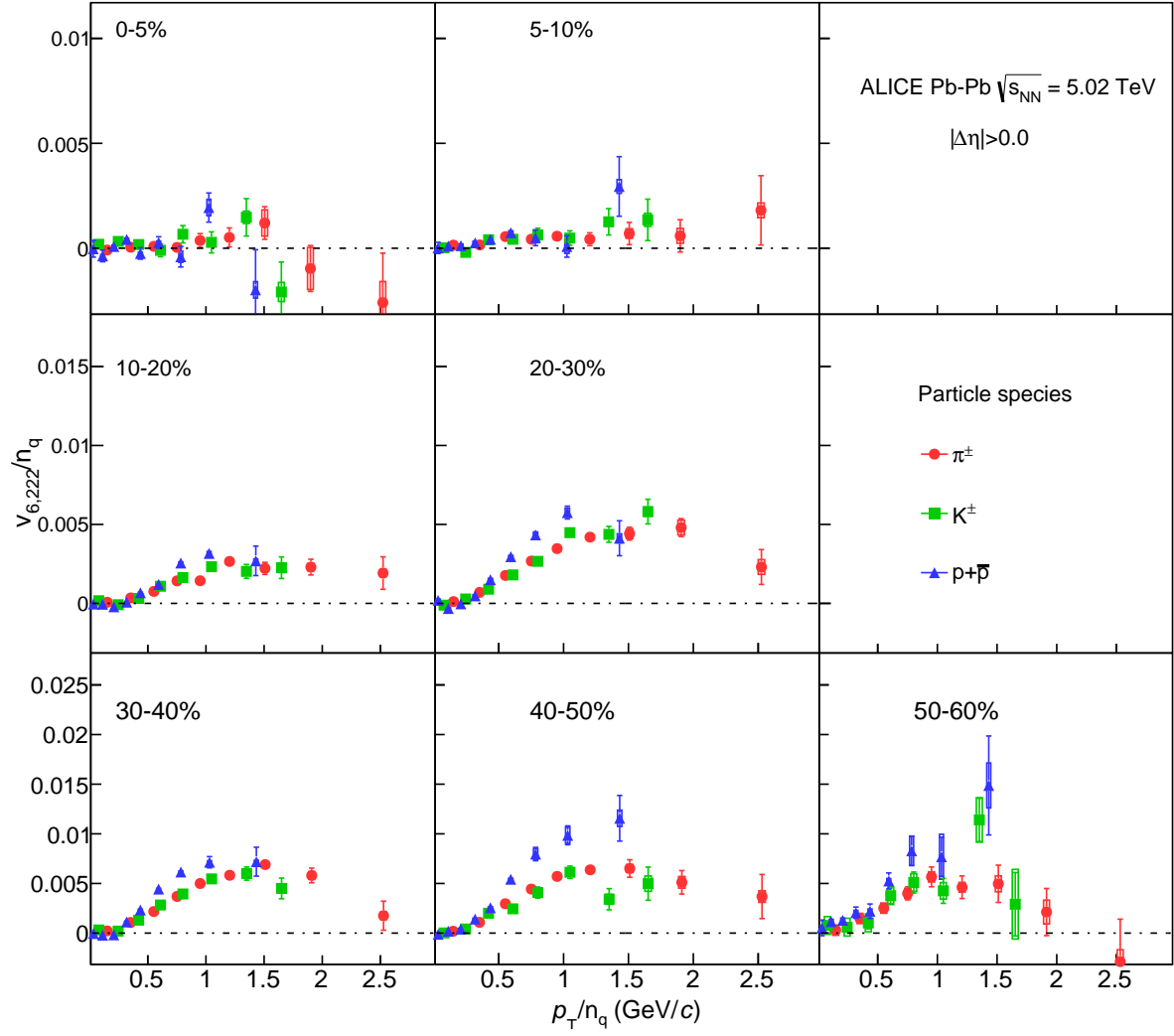


**Figure A.4:** The  $(m_T - m_0)/n_q$ -dependence of  $v_{6,222}/n_q$  for different particle species grouped into different centrality intervals of Pb–Pb collisions  $\sqrt{s_{NN}} = 5.02$  TeV